

1
2
3
4
5 **MJO and Convectively Coupled Equatorial Waves Simulated by CMIP5 Climate Models**
6

7
8 Meng-Pai Hung^{1,2}, Jia-Lin Lin³, Wanqiu Wang¹, Daehyun Kim⁴, Toshiaki Shinoda⁵,
9 and Scott J. Weaver¹
10

11
12 ¹Climate Prediction Center, NCEP/NWS/NOAA, College Park, Maryland

13 ²Wyle Information Systems, McLean, Virginia

14 ³Department of Geography, The Ohio State University, Columbus, Ohio

15 ⁴Lamont-Doherty Earth Observatory, Columbia University, Palisades, New York

16 ⁵Naval Research Laboratory, Stennis Space Center, Mississippi
17
18
19
20
21
22
23
24
25
26
27
28
29
30
31
32

33 Submitted to *J. Climate*

34 July 2012
35
36

37 Corresponding author address: Dr. Meng-Pai Hung
38 Climate Prediction Center, NCEP/NWS/NOAA
39 5830 University Research Court, College Park, Maryland 20740
40 Email: mengpai.hung@noaa.gov

Abstract

This study evaluates the simulation of Madden-Julian Oscillation (MJO) and convectively coupled equatorial waves (CCEWs) in 20 Coupled Model Intercomparison Project Phase 5 (CMIP5) models participating in the Inter-governmental Panel on Climate Change (IPCC) Fifth Assessment Report (AR5), and compares the results with the simulation of CMIP Phase 3 (CMIP3) models participating in the IPCC Fourth Assessment Report (AR4). The results show that the CMIP5 models improve significantly over the CMIP3 models in simulating the tropical intraseasonal variability. The CMIP5 models generally produce larger total intraseasonal (2-128 day) variance of precipitation than the CMIP3 models, as well as larger variances of Kelvin, equatorial Rossby (ER), mixed Rossby-gravity (MRG), and eastward inertio-gravity (EIG) waves. Almost all models have signals of the CCEWs, with Kelvin and MRG-EIG waves especially prominent. The phase speeds, as scaled to equivalent depths, are close to the observed value in 10 of the 20 models, suggesting that these models are producing sufficient reduction in their “effective static stability” by diabatic heating.

The CMIP5 models generally produce larger MJO variance than the CMIP3 models, and a more realistic ratio between the variance of the eastward MJO and that of its westward counterpart. About one third of the CMIP5 models generate the spectral peak of MJO precipitation between 30-70 days, but the model MJO period tends to be longer than observations as part of an over-reddened spectrum, which in turn is associated with too strong persistence of equatorial precipitation. Only one of the 20 models is able to simulate a realistic eastward propagation of the MJO.

1. Introduction

The tropical intraseasonal variability plays an important role in the global climate system and is a key source of untapped predictability in both the tropics and extratropics (e.g. Wheeler and Kiladis 1999, hereafter WK; Wheeler and Weickmann 2001; Schubert et al. 2002; Waliser et al. 2003a; Zhang 2005; Lin et al. 2006). The dominant tropical intraseasonal modes include the Madden-Julian Oscillation (MJO, Madden and Julian 1971) and convectively coupled Kelvin, equatorial Rossby, mixed Rossby-gravity (MRG), eastward inertio-gravity (EIG), and westward inertio-gravity (WIG) waves (Takayabu 1994; WK). These modes strongly affect the tropical weather such as the onset and breaks of different monsoon systems (e.g. Yasunari 1979; Wheeler and McBride 2005) and formation of tropical cyclones in all ocean basins (e.g. Liebmann et al. 1994; Maloney and Hartmann 2001; Besafi and Wheeler 2006; Klotzbach 2010). On longer time scales, the tropical intraseasonal modes are influential in the triggering and termination of El Nino/Southern Oscillation (ENSO) events (Kessler et al. 1995; Takayabu et al. 1999; Bergman et al. 2001). The presence of intraseasonal variability in the initial state of a seasonal forecast system can substantially modulate the prediction of ENSO (Wang et al. 2011). As a strong tropical heating source, the MJO also drives teleconnections to the extratropics affecting precipitation events in North and South Americas (e.g. Mo and Higgins 1998; Jones and Schemm 2000) and both the Arctic and Antarctic Oscillations (Miller et al. 2003; Carvalho et al. 2005).

Unfortunately, poor simulation of the tropical intraseasonal variability has been a pervasive problem in the last several generations of global climate models (Slingo et al. 1996; Lin et al. 2006; Zhang et al. 2006; Sperber and Annamalai 2008; Kim et al. 2009; Weaver et al. 2011). The Atmospheric Model Intercomparison Project (AMIP) study by Slingo et al. (1996) found that no

86 model has captured the dominance of the MJO in space-time spectral analysis found in
87 observations, and nearly all have relatively more power at higher frequencies (<30 days) than in
88 observations. Lin et al. (2006) evaluated the tropical intraseasonal modes in 14 GCMs
89 participating in the Coupled Model Intercomparison Project Phase 3 (CMIP3) used to inform the
90 Inter-governmental Panel on Climate Change (IPCC) Fourth Assessment Report (AR4). They
91 found that the total intraseasonal (2-128 day) variance of precipitation is too weak in most of the
92 models. About half of the models have signals of convectively coupled equatorial waves, with
93 Kelvin and MRG-EIG waves especially prominent. However, the variances are generally too
94 weak for all wave modes except the EIG wave, while the phase speeds are generally too fast,
95 being scaled to excessively deep equivalent depths. Interestingly, this scaling is consistent within
96 a given model across modes, in that both the symmetric and antisymmetric modes scale similarly
97 to a certain equivalent depth. Excessively deep equivalent depths suggest that these models may
98 not have a large enough reduction in their “effective static stability” by diabatic heating. The
99 MJO variance approaches the observed value in only two of the 14 models, however is less than
100 half of the observed value in the other 12 models. The ratio between the eastward MJO variance
101 and the variance of its westward counterpart is too small in a majority of the models, which is
102 consistent with the lack of highly coherent eastward propagation of the MJO in these model
103 simulations. Moreover, the MJO variance in 13 of the 14 models does not derive from a
104 pronounced spectral peak, however usually comes as a result of an over-reddened spectrum,
105 which in turn is associated with too strong persistence of equatorial precipitation. The two
106 models that arguably do best at simulating the MJO are the only ones having convective
107 closures/triggers linked in some way to moisture convergence.

Recently, there have been targeted efforts in improving the simulation of tropical intraseasonal variability in global climate models. Factors found important for increased fidelity of the simulation of tropical intraseasonal variability include moisture convective trigger (e.g. Wang and Schlesinger 1999; Lin et al. 2008; Kim and Kang 2012; Kim et al. 2012) or diluted CAPE closure (Subramanian et al. 2011; Zhou et al. 2012), interaction between deep and shallow convection (Zhang and Song 2009), interaction between deep convection and stratiform precipitation (Fu and Wang 2009; Seo and Wang 2010), vertical heating profile (Li et al. 2009), convective momentum transport (Deng and Wu 2010; Zhou et al. 2012), cloud-radiation feedback (Lin et al. 2007; Kim et al. 2011), and time-mean state (Sperber and Annamalai 2008; Kim et al. 2009).

In preparation for the IPCC Fifth Assessment Report (AR5), nearly two dozen international climate modeling centers conducted simulations for the fifth phase of the Coupled Model Intercomparison Project (CMIP5; Taylor et al. 2012). The CMIP5 simulations include a comprehensive set of long-term simulations for both the 20th century's climate and various climate change scenarios for the 21st century. Scientific questions that arose during preparation of the IPCC AR4 will be addressed through the CMIP5, which is a standard protocol providing a framework for climate change experiments and simulations for assessment in the IPCC AR5. Compared to the CMIP3 models, the CMIP5 models generally have higher resolutions and improved physical schemes. Some of the CMIP5 models also evolve from "climate system models" to "earth system models" that include biogeochemical components and time-varying carbon fluxes between the ocean, atmosphere, and terrestrial biosphere. Therefore, it is of great interest and important to evaluate general performance of the new generation of climate models used for climate projections in the IPCC AR5. This study focuses on the simulations of tropical

intraseasonal variability in this new generation of climate models and assesses the effect of the updated physical processes, higher resolution, and interactive carbon cycle.

The models and validation datasets used in this study are described in section 2. The diagnostic methods are described in section 3. Results are presented in section 4. A summary and discussion are given in section 5.

2. Models and validation datasets

For direct comparison with Lin et al. (2006), we use eight years of historical simulations from 20 coupled GCMs in CMIP5. Table 1 shows the model names and acronyms. For each model, we use eight years of daily mean surface precipitation. The model simulations are validated using multiple observational datasets. To bracket the uncertainties associated with precipitation measurements/retrievals, we use two different precipitation datasets (as in Lin et al. 2006.) that cover eight years from 1997 to 2004. The first set is the daily Geostationary Operational Environment Satellite (GOES) Precipitation Index (GPI; Janowiak and Arkin 1991) with a horizontal resolution of 2.5° latitude by 2.5° longitude, which is retrieved based on infrared (IR) measurements from multiple geostationary satellites. The second eight year set is the daily Global Precipitation Climatology Project (GPCP) 1° daily (1DD) precipitation (Huffman et al. 2001) with a horizontal resolution of 1° longitude by 1° latitude.

3. Method

The methods used in this study are identical to those used in Lin et al. (2006) for evaluating the CMIP3 models, which followed the methodology of WK. We will briefly outline this procedure here, and refer the reader to Lin et al. (2006) and WK for further details. First, in order

to identify the dominant intraseasonal modes, space-time spectra of daily tropical precipitation were obtained for the eight years of model data used in this study and compared with the results of eight years of observed precipitation estimates from the GPI and 1DD datasets. The model and validation precipitation data were first averaged to a zonal resolution of 5 degrees longitude, and then the 0°N - 15°N mean and 0°N - 15°S mean were calculated. The symmetric component is defined as the sum of 0°N - 15°N mean and 0°N - 15°S mean divided by 2, while the anti-symmetric component is defined as the difference between 0°N - 15°N mean and 0°N - 15°S mean divided by 2. Then the wavenumber –frequency spectra were calculated for both the symmetric and anti-symmetric components. Secondly, the definitions of Kelvin, ER, MGR, EIG and WIG modes are as in WK (see their Fig. 6), and were isolated using the same method, each mode was isolated by filtering in the wavenumber-frequency domain (see Fig. 6 of WK for the defined regions of filtering for each wave), and the corresponding time series were obtained by an inverse space-time Fourier transform. Thirdly, the MJO is defined as significant rainfall variability in eastward wavenumber 1-6 and in the period range of 30-70 days. To isolate the MJO mode, we used an inverse space-time Fourier transform to get the time series of the eastward wavenumber 1-6 component, which includes all available frequencies. Then these time series were filtered using a 365-point 30-70-day Lanczos filter (Duchan 1979), whose response function is shown in Fig. 2 of Lin et al. 2006). Since the Lanczos filter is nonrecursive, 182 days of data were lost at each end of the time series (364 days in total). The resultant eastward wavenumber 1-6, 30-70-day anomaly is hereafter referred to as the MJO anomaly. The variance of the MJO anomaly was also compared with the variance of its westward counterpart, that is, the westward wavenumber 1-6, 30-70-day anomaly, which is isolated using the same method as above.

It is important to note that we only focus on the intraseasonal variability, which propagates eastward and amplifies to a seasonal maximum on the equator in boreal winter and spring, when climatological convection and warm SST cross the equator (Salby and Hendon 1994; Zhang and Dong 2004; Wheeler and Hendon 2004). Analysis of the Boreal Summer Intraseasonal Oscillation (BSIO; e.g. Yasunari 1979; Knutson et al. 1986; Kemball-Cook and Wang 2001; Lawrence and Webster 2002; Straub and Kiladis 2003; Waliser et al. 2003b; among many others), which has a major northward propagating component and has its maximum variance in the Asian monsoon region, is beyond the scope of this study.

4. Results

a. Climatological precipitation in the equatorial belt

Previous observational studies indicate that the intraseasonal variance of convection is highly correlated with time-mean convective intensity (e.g., WK; Hendon et al. 1999). Therefore, we first examine the eight-year time-mean precipitation along the equatorial belt, especially over the Indo-Pacific warm pool region, where most of the convectively coupled equatorial waves have the largest variance (WK). Figure 1a shows the annual mean precipitation versus longitude averaged between 15°N and 15°S. To focus on the large-scale features, we smoothed the data zonally to retain only zonal wavenumbers 0-6. Similar to the CMIP3 models, those from the CMIP5 reproduce the basic feature of observed precipitation, with primary maximum over the Indo-Pacific warm pool region, and two secondary maxima over Central/South America and Africa. The magnitude of the precipitation over the warm pool in all models is close to that in the observations. Compared to the CMIP3 models, a notable improvement in the CMIP5 models is more realistic precipitation over the eastern Indian Ocean. However, within the warm pool region, only five models (CanESM2, CanCM4, CSIRO, INMCM4, and FGOALS) reproduce the

local minimum of precipitation over the Maritime Continent. Outside the warm pool region, the common biases for the CMIP3 models of excessive rainfall throughout the eastern Pacific and insufficient rainfall over Central/South America still exist in most of the CMIP5 models.

When the precipitation is averaged over a narrower belt closer to the equator between 5°N and 5°S, models show a larger scatter in their performance, especially over the Indo-Pacific warm pool (Fig. 1b). Some models (e.g., IPSL-5BL, MIROC4h, HadG2-ES, and MRI3) produce much greater precipitation over the western Pacific than over the eastern Indian Ocean, a feature that is not observed. On the other hand, several other models (CSIRO, INMCM4, IPSL-5AL, and IPSL-5AM) show too strong precipitation over the eastern Indian Ocean, and too weak precipitation over the western Pacific, which is significantly smaller than their corresponding 15°N-15°S average (Fig. 1a). This is caused by the double-ITCZ pattern in their horizontal distributions (not shown), and the problem is even worse in the CMIP5 simulations than in the CMIP3 models. Outside the warm pool region, all models produce much larger precipitation than observations over the western Indian Ocean and eastern Pacific, and all models except CSIRO simulate excessive precipitation over the Atlantic Ocean.

In short, the climatological precipitation over the Indo-Pacific warm pool is reasonably simulated by the CMIP5 climate models, except that several models (CSIRO, INMCM4, IPSL-5AL, and IPSL-5AM) produce too weak precipitation on the equator in the western Pacific due to their double-ITCZ problem. The CMIP5 models generally produce better annual mean precipitation over the Indo-Pacific warm pool region than the CMIP3 models. However, the simulations in the western Indian Ocean, eastern Pacific, South America and the Atlantic Ocean still need to be improved.

b. Total intraseasonal (2-128 day) variance and raw space-time spectra

Figures 2a and 2b show the total variance of the 2-128-day precipitation anomaly along the equator averaged between 15°N-15°S and 5°N-5°S, respectively. The CMIP5 models generally simulate larger total intraseasonal variance than the CMIP3 models. About half of the CMIP5 models produce total intraseasonal variance that is close to or larger than observations over the Indo-Pacific warm pool, especially the western Pacific. For CMIP3, only two or three models simulated variances that are close to observations (Lin et al. 2006). There is a tendency for the CMIP5 models to have larger variance over the western Pacific than over the Indian Ocean, which is consistent with their tendency to have larger annual mean precipitation over the western Pacific (Fig. 1), and was also a feature for the CMIP3 models.

Figure 3 shows the raw symmetric wavenumber-frequency power spectra of equatorial precipitation. Here we present only spectra of the symmetric component, as characteristics of the anti-symmetric spectra are similar to those of the symmetric spectra. Note that the powers are drawn in log-scale. Figure 3 demonstrates two points. First, the models spectra tend to be over-reddened than observations with less power at periods shorter than 6 days, although a few models (CanESM2, CanCM4, CNRM-CM5, and MIROC4h) have powers comparable to observation at the short time scales. Secondly, for the MJO time scale (period > 30 days), nine of the 20 models (CNRM-CM5, CSIRO, IPSL-5BL, FGOALS, MIROC5, HadCM3, MPI-E-L, MRI3, and NorE1-M) exhibit power that is comparable to observations. These models also tend to simulate stronger eastward power than westward at the MJO time scale, which is an improvement over the CMIP3 model simulations (Lin et al. 2006).

c. Dominant intraseasonal modes

In Figure 4 and Figure 5, symmetric and anti-symmetric waves are identified by removing background spectra from the raw symmetric and anti-symmetric spectra, respectively. The waves include the MJO and convectively coupled Kelvin, ER, MRG, EIG and WIG waves. The CMIP5 models improve significantly over the CMIP3 models in simulating the signals of MJO and convectively coupled equatorial waves. Almost all CMIP5 models are able to simulate convectively coupled equatorial waves, especially the Kelvin and the MRG-EIG waves, although the Kelvin wave signal is not distinctive in IPSL-5BL and the MRG-EIG waves are not well simulated by INMCM4 and IPSL-5AM. Moreover, the equivalent depth of the waves in 10 of the 20 models (CanESM2, CanCM4, CCSM4, FGOALS, MIROC5, HadCM3, HadG2-CC, HadG2-ES, MPI-E-L, and NorE1-M) is around the observed value of 25 m, although it is too deep in five models (INMCM4, IPSL-5AL, IPSL-5AM, MIROC-E, and MIROC-EC) and too shallow in two models (CNRM-CM5, and MRI3). These are encouraging results because only half of the CMIP3 models have signals of convectively coupled equatorial waves, and the equivalent depth of the waves was generally too high (Lin et al. 2006). As in the CMIP3 models, the equivalent depth of waves is consistent within one model. As discussed in Lin et al. (2006), correct equivalent depth suggests that the models are producing a large enough reduction in their “effective static stability” from diabatic heating.

About half of the CMIP5 models (CNRM-CM5, CSIRO, IPSL-5AL, IPSL-5BL, MIROC5, HadCM3, MPI-E-L, MRI3, and NorE1-M) exhibit the spectral peak of the MJO, and powers of eastward propagating components near the MJO time scale are more distinctive than that of westward propagating ones. This is promising when compared to the results of CMIP3 models,

where 4 out of 14 models showed such features, and it suggests that there has been progress in MJO modeling between CMIP3 and CMIP5.

When a model displays signals of a certain wave mode in Figs. 4 and Fig. 5, it means that the variance of that wave mode stands out above the background spectra (i.e., a high signal-to noise ratio), but the absolute value of the variance of that wave may not be large. Therefore, it is of interest to look at the absolute values of the variance of each wave mode. Figures 6a-e, show the variances of the Kelvin, ER, MRG, EIG, and WIG modes along the equator averaged between 15°N and 15°S. For the Kelvin mode (Fig. 6a), the CMIP5 models generally show larger variance than the CMIP3 models although the CMIP5 model variances are still smaller than observations. Some models (CCSM4, CNRM-CM5, FGOALS, MIROC4h, MIP-E-L, MRI3, and NorE1-M) even capture the observed longitudinal distribution. For the ER mode (Fig. 6b), the CMIP5 models generally produce larger variances than the CMIP3 models with two models (FGOALS and MPI-E-L) faithfully reproducing the observed magnitude and longitudinal distribution of the variance. For the MRG mode (Fig. 6c), which is important for tropical cyclone genesis, again the CMIP5 models generally simulate stronger variances than CMIP3 models with their largest amplitude over the Indo-Pacific region as in observations, however all modes produce too small variances although their largest amplitudes are located over the Indo-Pacific region, which is same as in observations. For the EIG mode (Fig. 6d), there is a large scatter in the simulated variances. Only three models (CNRM-CM5, IPSL-5AM, and HadG2-ES) produce nearly realistic magnitude and are able to capture the observed two maxima over the warm pool region. Several models (IPSL-5BL, FGOALS, MPI-E-L, and MRI3) produce overly strong variances, while others (e.g. INMCM4, IPSL-5AL, MIROC-E, and MIROC-EC) simulate overly

weak variances. For the WIG mode (Fig. 6e), all models simulate too weak variance except CNRM-CM5, which produces nearly realistic variance over the western Pacific.

d. Variance of the MJO mode

In this section, the focus turns to the MJO mode, specifically the daily variance in the MJO window of eastward wavenumbers 1-6 and periods of 30-70 days. Figure 7a shows the variance of the MJO anomaly along the equator averaged between 15°N and 15°S. The CMIP5 models generally produce much larger MJO variance than the CMIP3 models. For CMIP3, there were only two models with MJO variance larger than half of the observed values, while for CMIP5, there are seven models (CNRM-CM5, CSIRO, IPSL-5BL, FGOALS, MRI-3, MIROC5, and MPI-E-L) with MJO variance larger than half of the observed values over eastern Indian Ocean and/or western Pacific. Most of models produce the maximum variance over the eastern Indian Ocean. This is a significant improvement of the global climate models since too weak precipitation variance in the MJO wavenumber-frequency band has been a long-standing problem in GCMs, in spite of the fact that many of these models have reasonable values of zonal wind variance. From the viewpoint of weather and climate prediction, a realistic MJO precipitation signal is highly desirable because it is the latent heat released by precipitation that drives teleconnections to the subtropics and extratropics and leads to useful predictability.

The 15°N-15°S belt, analyzed above is a wide belt. As shown by Wang and Rui (1990), eastward-propagating MJO precipitation events occur most often on the equator, with the frequency of occurrence decreasing away from the equator. Therefore, it is of interest to see if the models capture this equatorial maximum of MJO variance. Figure 7b is same as Fig. 7a except precipitation averaged between 5°N and 5°S. For both of the two observational datasets,

the variance of the 5°N-5°S average is about twice as large as that of the 15°N-15°S average. CNRM-CM5 and IPSL-5BL produce very realistic MJO precipitation variance, with the variance of CNRM-CM5 particularly agrees with GPI dataset throughout the entire Indian Ocean and the western Pacific. Three other models (CSIRO, MPI-E-L, and MRI3) also simulate large MJO variance close to the equator, although the models with a double-ITCZ pattern produce large variance only over the Indian Ocean but not the western Pacific.

In addition to the variance of the eastward MJO, another important index for evaluating the MJO simulation is the ratio between the variance of the eastward MJO and that of its westward counterpart, that is, the westward wavenumber 1-6, 30-70-day mode, which is important for the zonal propagation of tropical intraseasonal oscillation. Figure 8 shows the ratio between the eastward and westward variance averaged over an Indian Ocean box between 5°N-5°S and 70°-100°E (panel a), and a western Pacific box between 5°N-5°S and 140°-170°E (panel b). Over the Indian Ocean (Fig. 8a), the eastward MJO variance roughly triples the westward variance in observations. The CMIP5 models generally produce a larger ratio than the CMIP3 models, with two of the 20 models (CNRM-CM5 and CSIRO) simulating a realistic or too large ratio, six other models (IPSL-5AL, IPSL-5AM, IPSL-5BL, MIROC5, MPI-E-L, MRI3, and NorE1-M) generating a ratio larger than 2, and no model producing a ratio smaller than one (i.e., westward variance dominates over eastward variance). Over the western Pacific (Fig. 8b), again, the eastward MJO variance nearly triple its westward counterpart in observations. Many models generally perform poorly over the western Pacific with the ratio less than one, which may be due to the double-ITCZ problem in many of the models or being unable to simulate the propagation from the Indian Ocean to the western Pacific. Only two models (CNRM-CM5 and FGOALS) produce a nearly realistic ratio, while seven models generate a ratio smaller than one.

339 The competition between the eastward MJO variance and its westward counterpart largely
340 determines the zonal propagation characteristics of the tropical intraseasonal oscillation. A useful
341 method for evaluating the MJO simulation is to look at the propagation of the 30-70-day filtered
342 anomaly of the raw precipitation data, which includes all wavenumbers (zonal mean, eastward
343 wavenumbers 1-6, westward wavenumbers 1-6, eastward wavenumbers 7 and up, westward
344 wavenumbers 7 and up), to ascertain if the MJO mode (the eastward wavenumbers 1-6 mode)
345 dominates over other modes, as is the case in the observations (e.g., Weickmann et al. 1985,
346 1997; Kiladis and Weickmann 1992; Lin and Mapes 2004). Since the tropical intraseasonal
347 oscillation is dominated by zonally asymmetric, planetary-scale phenomena, the competition is
348 mainly between the MJO and its westward counterpart – the westward wavenumbers 1-6
349 component. Figure 9 shows the lag correlation of the 30-70-day precipitation anomaly averaged
350 between 5°N and 5°S with respect to itself at 0°, 85°E. Both observational datasets show
351 prominent eastward-propagating signals of the MJO, with a phase speed of about 7 m s⁻¹. The
352 models display a wide range of propagation characteristics that are consistent with the ratio
353 between the eastward MJO variance and its westward counterpart shown in Fig. 8a. The two
354 models with a realistic or too large ratio (CNRM-CM5 and CSIRO) show a highly coherent
355 eastward-propagating signal. The phase speed is slightly slower than observations in CNRM-
356 CM5, however is much slower than observations in CSIRO. The seven models (IPSL-5AL,
357 IPSL-5AM, IPSL-5BL, MIROC5, MPI-E-L, MRI3, and NorE1-M) with the eastward/westward
358 ratio in the Indian Ocean being larger than two but smaller than in observations show only
359 discernable eastward-propagating signals and the phase speeds tend to be too slow. Other models
360 with the ratio being nearly equal to one show standing oscillations. The results are poor when

using a western Pacific reference point (not shown), which is consistent with the worse eastward/westward ratio in Fig. 8b.

Next we apply a more detailed scrutiny of the MJO precipitation variance by looking at the shape of the power spectrum. Figure 10 shows the normalized spectra of the eastward wavenumber 1-6 component at 0° , 85°E . Both of the observational datasets show prominent spectral peaks between 30-and 70-day periods, with the power of 1DD lower than that of GPI. Compared to the CMIP3 models, a big improvement of the CMIP5 models is that five models (CNRM-CM5, IPSL-5AL, IPSL-5BL, CSIRO, and MIROC5) produce the 30-70 day spectral peak of the MJO, while for CMIP3 only two models were able to generate the spectral peak of the MJO. However, the period of MJO in four of the above five CMIP5 models is between 45-70 days, which is longer than in observations. The only model showing a nearly correct MJO period is IPSL-5BL. Moreover, the normalized spectra of the models are over-reddened with too much variance at the low frequency end, suggesting the model precipitation is more persistent than observation. We'll come back to this point in the next subsection.

e. Autocorrelation of precipitation

The autocorrelation analysis is similar as in Lin et al. (2006). For the first-order Markov process (Equation (1) in Lin et al. 2006), the redness of the spectrum is determined by its lag-one autocorrelation ρ (Equation (2) in Lin et al. 2006). Therefore, we plot in Fig. 11 the autocorrelation function of precipitation at 0° , 85°E . Both observational datasets have a ρ of about 0.7. The CMIP5 models generally produce a smaller value of ρ than CMIP3 models. Three of the twenty CMIP5 models (MIROC4H, MIROC-E, and MIROC-EC) have a ρ similar to or smaller than the observed value. Moreover, the autocorrelation values at longer time lags are

generally smaller and more realistic in the CMIP5 models than in the CMIP3 models, which is consistent with the better MJO spectral peaks in the CMIP5 models. Nevertheless, all the CMIP5 models analyzed in this study have too large values of ρ at the lag beyond 5 days, suggesting that they have too strong persistence of precipitation, which is closely associated with their overreddened spectra. This may contribute to the too long MJO period (50-90 days) and too slow MJO phase speed in those models (Figs. 9 and 10). In addition to the shape of the spectrum, the precipitation persistence also affects the modes at the high-frequency end of the spectrum, such as the WIG mode (the 2-day wave). A too strong persistence tends to suppress the high-frequency modes and may contribute too weak variances of these modes in the models (Fig. 6e).

5. Summary and discussions

This study evaluates the tropical intraseasonal variability, especially the MJO and CCEWs, simulated by 20 CMIP5 coupled GCMs. The results are compared with the simulations of 14 CMIP3 models evaluated by Lin et al. (2006). The results show that the CMIP5 models improve significantly over the CMIP3 models in simulating the tropical intraseasonal variability. The CMIP5 models generally produce larger total intraseasonal (2-128 day) variance of precipitation than the CMIP3 models, as well as larger variances of Kelvin, ER, MRG and EIG waves. About half of the models have signals of convectively coupled equatorial waves, with Kelvin and MRG-EIG waves especially prominent, and the phase speeds are generally realistic, being scaled to correct equivalent depths. Correct equivalent depths suggest that these models are producing large enough reduction in their “effective static stability” by diabatic heating.

The CMIP5 models generally produce larger MJO variance than the CMIP3 models, and a more realistic ratio between the eastward MJO variance and the variance of its westward

counterpart. About one third of the CMIP5 models generate the spectral peak of MJO precipitation between 30-70 days. However, the phase speeds of the model MJO tend to be too slow and the period is longer than observations as part of an over-reddened spectrum, which in turn is associated with too strong persistence of equatorial precipitation.

For CMIP5, several modeling centers provided a series of models with varying complexity and spatial resolutions ranging from Atmosphere-Ocean global climate system models (AOGCMs), to more comprehensive earth system models (ESMs), including some that are coupled to chemical models. They are usually using the same atmospheric model but sometime with different resolutions. Among the 20 models we analyzed, we have four such groups evolving “standard models” (i.e., AOGCMs) and earth system models (ESMs): (1) CanCM4 and CanESM2, (2) IPSL-CM5A-LR and IPSL-CM5A-MR, (3) MIROC5, MIROC-E, and MIROC-EC, and (4) HadCM3, Had-G2-CC, and Had-G2-ES. Within each group, there is on significant difference in the skill of simulating the MJO or convectively coupled equatorial waves, suggesting the simulated tropical intraseasonal variability is not sensitive to model resolution or chemical processes.

Our results show that the too strong persistence of precipitation in many CMIP3 models has been reduced in the CMIP5 models, which may contribute to the improvement of model simulations of tropical intraseasonal variability. However, the persistence of precipitation in many CMIP5 models is still larger than observations (Fig. 10). The weak persistence of precipitation in observations may be associated with the well-known self-suppression processes in deep convection, with convective downdrafts reducing the entropy of the boundary layer and the mesoscale downdrafts reducing the entropy of the lower troposphere, and diluted convective updrafts being sensitive to the change of boundary layer and lower troposphere entropy (see

more detailed discussion in Lin et al. 2006 and references therein). The current GCMs have not included all the above self-suppression processes in deep convection, especially the effects of mesoscale downdrafts. Better representation of these physical processes may help to further improve the simulation of tropical intraseasonal variability.

Many CMIP5 models are able to simulate much larger MJO variance than the CMIP3 models, and can even produce the 30-70 day spectral peak of MJO. These are notable improvements in MJO modeling. Models generating large MJO variance and the 30-70 day spectral peak (e.g., CNRM-CM5, CSIRO, IPSL-5BL, and MIROC5) have different types of convective closure (Table 1), suggesting that better simulations of MJO variance and spectral peak are not linked to a specific type of convective closure. However, the eastward propagation of MJO is still difficult to reproduce. The only model that can produce a realistic eastward propagation of MJO (CNRM-CM5) is the only model using a moisture-convergence-type closure for convection, suggesting that the low-level moisture convergence may play an important role in the MJO's eastward propagation.

Acknowledgments

We acknowledge the World Climate Research Programme's Working Group on Coupled Modeling, which is responsible for CMIP, and we thank the climate modeling groups (listed in Table 1 of this paper) for producing and making available their model output. For CMIP the U.S. Department of Energy's Program for Climate Model Diagnosis and Intercomparison provides coordinating support and led development of software infrastructure in partnership with the Global Organization for Earth System Science Portals. J.-L. Lin was supported by NOAA Climate Program Office Modeling, Analysis, Predictions and Projections (MAPP) Program as

453 part of the CMIP5 Task Force under grant #GC10-400, NASA MAP Program, and NSF Grant
454 ATM-0745872. T. Shinoda is supported by NOAA CPO MAPP and ESS (GC10-400,
455 NA11OAR4310110), and ONR/LASP project (Program Element 601153N). We would like to
456 thank Chidong Zhang for his important encouragement to this work, and Haibo Liu for his help
457 in downloading the IPCC AR5 data.

458

References

- Bergman, J. W., H. H. Hendon, K. M. Weickmann, 2001: Intraseasonal Air-Sea Interactions at the Onset of El Nino. *J. Climate*, **14**, 1702-1719.
- Carvalho, L. M. V., C. Jones, and T. Ambrizzi. 2005: Opposite Phases of the Antarctic Oscillation and Relationships with Intraseasonal to Interannual Activity in the Tropics during the Austral Summer. *J. Climate*, **18**, 702–718.
- Chikira, M., and M. Sugiyama, 2010: A cumulus parameterization with state-dependent entrainment rate. Part I: Description and sensitivity to temperature and humidity profiles. *J. Atmos. Sci.*, **67**, 2171–2193.
- Collins, W. J., and Coauthors, 2011: Development and evaluation of an Earth-system model – HadGEM2. *Geosci. Model Dev.*, **4**, 1051–1075. doi:10.5194/gmd-4-1051-2011.
- Deng, L., X. Wu, 2010: Effects of Convective Processes on GCM Simulations of the Madden-Julian Oscillation. *J. Climate*, **23**, 352–377.
- Duchan, C.E., 1979: Lanczos filtering in one and two dimensions. *J. Appl. Meteor.*, **18**, 1016-1022.
- Fu, X., and B. Wang, 2009: Critical roles of the stratiform rainfall in sustaining the Madden-Julian Oscillation: GCM experiments. *J. Climate*, **22**, 3939–3959.
- Grandpeix, J.-Y., J.-P. Lafore, 2010: A Density Current Parameterization Coupled with Emanuel’s Convection Scheme. Part I: The Models. *J. Atmos. Sci.*, **67**, 881–897.
- Hendon, H. H., C. Zhang, and J. D. Glick, 1999: Interannual variation of the MJO during austral summer. *J. Climate*, **12**, 2538-2550.
- Higgins, R. W., J.-K. E. Schemm, W. Shi, and A. Leetmaa, 2000: Extreme Precipitation Events in the Western United States Related to Tropical Forcing. *J. Climate*, **13**, 793-820.
- Huffman, G.J., R.F. Adler, M.M. Morrissey, S. Curtis, R. Joyce, B. McGavock, and J. Susskind, 2001: Global precipitation at one-degree daily resolution from multi-satellite observations. *J. Hydrometeor.*, **2**, 36-50.
- Janowiak, J. E., and P. A. Arkin, 1991: Rainfall variations in the Tropics during 1986- 1989, as estimated from observations of cloud-top temperatures. *J. Geophys. Res.*, **96** (Suppl.), 3359-3373.
- Jones, C., and J.-K. E. Schemm, 2000: The influence of intraseasonal variations on medium-range weather forecasts over South America. *Mon. Wea. Rev.*, **128**, 486–494.

490 Jones, C. D., and Co-authors, 2011: The HadGEM2-ES implementation of CMIP5 centennial
491 simulations. *Geosci. Model Dev.*, **4**, 543–570. doi:10.5194/gmd-4-543-2011.

492 Kessler, W. S., M. J. McPhaden, and K. M. Weickmann, 1995: Forcing of intraseasonal Kelvin
493 waves in the equatorial Pacific. *J. Geophys. Res.*, **100**, 10613–10631.

494 Kemball-Cook, S., and B. Wang. 2001: Equatorial Waves and Air–Sea Interaction in the Boreal
495 Summer Intraseasonal Oscillation. *J. Climate*, **14**, 2923–2942.

496 Kiladis, G. N., and K. M. Weickmann, 1992: Circulation anomalies associated with tropical
497 convection during northern winter. *Mon. Wea. Rev.*, **120**, 1900–1923.

498 Kim, D., A. H. Sobel, E. D. Maloney, D. M. W. Frierson, and I.-S. Kang, 2011: A systematic
499 Relationship between intraseasonal variability and mean state bias in AGCM simulations.
500 *J. Climate*, **24**, 5506–5520.

501 Kim, D., and Coauthors, 2009: Application of MJO simulation diagnostics to climate models. *J.*
502 *Climate*, **22**, 6413–6436.

503 Kim, D., A. H. Sobel, and I.-S. Kang, 2011: A mechanism denial study on the Madden-Julian
504 Oscillation, *J. Adv. Model. Earth Syst.*, **3**, M12007, doi:10.1029/2011MS000081.

505 Kim, D., and I.-S. Kang, 2012: A bulk mass flux convection scheme for climate model -
506 Description and moisture sensitivity. *Clim. Dyn.*, **38**, 411–429.

507 Kim, D., A. H. Sobel, A. D. Del Genio, Y. Chen, S. J. Camargo, M.-S. Yao, M. Kelley, and L.
508 Nazarenko, 2012: Tropical Intraseasonal Variability Simulated in the NASA GISS General
509 Circulation Model. *J. Climate*, **25**, 4641–4659.

510 Klotzbach, P. J., 2010: On the Madden-Julian oscillation – Atlantic hurricane relationship. *J.*
511 *Climate*, **23**, 282–293.

512 Knutson, T. R., and K. M. Weickmann, 1987: 30–60 Day atmospheric oscillations: Composite
513 life cycles of convection and circulation anomalies. *Mon. Wea. Rev.*, **115**, 1407–1436.

514 Knutson, T. R., K. M. Weickmann, and J. E. Kutzbach, 1986: Global-scale intraseasonal
515 oscillations of outgoing longwave radiation and 250 mb zonal wind during Northern
516 Hemisphere summer. *Mon. Wea. Rev.*, **114**, 605–623.

517 Lawrence, D. M., and P. J. Webster. 2002: The Boreal Summer Intraseasonal Oscillation:
518 Relationship between Northward and Eastward Movement of Convection. *J. Atmos. Sci.*,
519 **59**, 1593–1606.

520 Li, C., X. Jia, J. Ling, W. Zhou and C. Zhang, 2009: Sensitivity of MJO simulations to diabatic
521 heating profile. *Climate Dyn.*, **32**, 167–187.

522 Liebmann, B., H. H. Hendon, and J. D. Glick, 1994: The relationship between the tropical cyclones
523 of the western Pacific and Indian Oceans and the Madden-Julian oscillation. *J. Meteor. Soc.
524 Japan*, **72**, 401–411.

525 Lin, H. and G. Brunet, 2008: Forecast skill of the Madden-Julian Oscillation in two Canadian
526 atmospheric models. *Mon. Wea. Rev.*, **136**, 4130–4149.

527 Lin, J. L., and B. E. Mapes, 2004: Radiation budget of the tropical intraseasonal oscillation. *J.
528 Atmos. Sci.*, **61**, 2050–2062.

529 Lin, J. L., B. E. Mapes, M. H. Zhang and M. Newman, 2004: Stratiform precipitation, vertical
530 heating profiles, and the Madden-Julian Oscillation. *J. Atmos. Sci.*, **61**, 296–309.

531 Lin, J.-L., M. Zhang, and B. Mapes, 2005: Zonal Momentum Budget of the Madden–Julian
532 Oscillation: The Source and Strength of Equivalent Linear Damping. *J. Atmos. Sci.*, **62**,
533 2172–2188.

534 Lin, J.-L., and Co-authors, 2006: Tropical intraseasonal variability in 14 IPCC AR4 climate
535 models. Part I: Convective signals. *J. Climate*, **19**, 2665–2690.

536 Lin, J. L., D. Kim, M.-I. Lee, and I.-S. Kang, 2007: Effects of cloud-radiative heating on AGCM
537 simulations of convectively coupled equatorial waves. *J. Geophys. Res.*, **112**, D24107,
538 doi:10.1029/2006JD008291.

539 Lin, J. L., M.-I. Lee, D. Kim, I.-S. Kang, and D. M. W. Frierson, 2008e: Impact of convective
540 parameterization and moisture triggering on GCM-simulated convectively coupled
541 equatorial waves. *J. Climate*, **21**, 883–909.

542 Gent, P. R., and Coauthors, 2011: The community climate system model version 4. *J. Climate*,
543 **24**, 4973–4991.

544 Madden, R. A., and P. R. Julian, 1971: Detection of a 40–50 day oscillation in the zonal wind in
545 the tropical Pacific. *J. Atmos. Sci.*, **28**, 702–708.

546 Madden, R. A., and P. R. Julian, 1972: Description of global-scale circulation cells in the tropics
547 with a 40–50 day period. *J. Atmos. Sci.*, **29**, 1109–1123 .

548 Maloney, E. D., and D. L. Hartmann, 2000: Modulation of eastern North Pacific hurricanes by
549 the Madden–Julian oscillation. *J. Climate.*, **13**, 1451–1460.

550 Maloney, E. D., and D. L. Hartmann, 2001: The Madden-Julian Oscillation, Barotropic
551 Dynamics, and North Pacific Tropical Cyclone Formation. Part I: Observations. *J. Atmos.
552 Sci.*, **58**, 2545–2558 .

553 Mao, J.-Y., and L.-J. Li, 2012: An assessment of MJO and tropical waves simulated by different
554 versions of GAMIL model. *Atmos. Oceanic Sci. Lett.*, **5**, 26–31.

555 Martin, G. M., and Coauthors, 2011: The HadGEM2 family of Met Office Unified Model
556 Climate configurations. *Geosci. Model Dev.*, **4**, 723–757. doi:10.5194/gmd-4-723-2011.

557 Miller, A. J, S Zhou, and S.-K Yang, 2003: Relationship of the Arctic and Antarctic Oscillation
558 to outgoing longwave radiation. *J. Climate.*, **16**, 1583–1592.

559 Mo, K. C., and R. W. Higgins, 1998: Tropical Influences on California Precipitation. *J. Climate*,
560 **11**, 412–430.

561 Neale, R. B., J. H. Richter, and M. Jochum, 2008: The impact of convection on ENSO: From a
562 delayed oscillator to a series of events. *J. Climate*, **21**, 5904–5924.

563 Paegle, J. N., L. A. Byerle, and K. C. Mo, 2000: Intraseasonal Modulation of South American
564 Summer Precipitation. *Mon. Wea. Rev.*, **128**, 837–850.

565 Roundy P. E., 2008: Analysis of convectively coupled Kelvin waves in the Indian Ocean MJO. *J.*
566 *Atmos. Sci.*, **65**, 1342–1359.

567 Salby, M. L., and H. H. Hendon, 1994: Intraseasonal behavior of clouds, temperature, and
568 motion in the Tropics. *J. Atmos. Sci.*, **51**, 2207–2224.

569 Schubert, S., R. Dole, H.v.d. Dool, M. Suarez, and D. Waliser, 2002: Proceedings from a
570 workshop on "Prospects for improved forecasts of weather and short-term climate
571 variability on subseasonal (2 week to 2 month) time scales", 16–18 April 2002,
572 Mitchellville, MD, NASA/TM 2002-104606, vol. 23, pp. 171.

573 Slingo, J. M., and Coauthors, 1996: Intraseasonal oscillations in 15 atmospheric general
574 circulation models: Results from an AMIP diagnostic subproject. *J. Climate Dyn.*, **12**, 325–
575 357.

576 Seo, K.-H. and W. Wang, 2010: The Madden-Julian oscillation simulated in the NCEP Climate
577 System: The importance of stratiform heating. *J. Climate*, **23**, 4470–4793.

578 Sperber, K. R., and H. Annamalai, 2008: Coupled model simulations of boreal summer
579 intraseasonal (30–50 day) variability, Part 1: Systematic errors and caution on use of metric.
580 *Climate Dyn.*, **31**, 345–372.

581 Stockhause, M., H. Höck, F. Toussaint, and M. Lautenschlager, 2012: Quality assessment
582 concept of the World Data Center for Climate and its application to CMIP5 data. *Geosci.*
583 *Model Dev. Discuss.*, **5**, 781–802.

584 Straub, K. H., and G. N. Kiladis, 2003: Interactions between the Boreal Summer Intraseasonal
585 Oscillation and Higher-Frequency Tropical Wave Activity. *Mon. Wea. Rev.*, **131**, 945–960.

586 Subramanian, A. C., M. Jochum, A. J. Miller, R. Murtugudde, R. B. Neale, and D. E. Waliser,
587 2011: The Madden-Julian oscillation in CCSM4. *J. Climate*, **24**, 6261–6282.

588 Takayabu, Y. N., 1994: Large-scale cloud disturbances associated with equatorial waves. Part I:
589 spectral features of the cloud disturbances. *J. Meteor. Soc. Japan*, **72**, 433–448.

590 Takayabu, Y. N., T. Iguchi, M. Kachi, A. Shibata, and H. Kanzawa, 1999: Abrupt termination of
591 the 1997-98 El Nino in response to a Madden-Julian oscillation. *Nature*, **402**, 279-282.

592 Taylor, K. E., R. J. Stouffer, and G. A. Meehl, 2012: An overview of CMIP5 and the experiment
593 design. *Bull. Amer. Meteor. Soc.*, **93**, 485–497.

594 Tromeur, E. and W. B. Bosson, 2010: Interaction of tropical deep convection with the large-
595 scale circulation in the MJO. *J. Climate*, **23**, 1837–1853.

596 Voldin, E. M., N. A. Dianskii, and A. V. Gusev, 2010: Simulating present-day climate with the
597 INMCM4.0 coupled model of the atmospheric and oceanic general circulations. *Atmos.*
598 *Oceanic Phy.*, **46**, (4), 414–431.

599 Voldoire, A., and Coauthors, 2012: The CNRM-CM5.1 global climate model: description and
600 basic evaluation. *Climate Dyn.*, doi:10.1007/s00382-011-1259-6, online.

601 Waliser, D. E., K. M. Lau, W. Stern, C. Jones, 2003a: Potential Predictability of the Madden-
602 Julian Oscillation, *Bull. Amer. Meteor. Soc.*, **84**, 33-50.

603 Waliser, D. E., W. Stern, S. Schubert, K. M. Lau, 2003b: Dynamic Predictability of Intraseasonal
604 Variability Associated with the Asian Summer Monsoon, *Quart. J. Royal Meteor. Soc.*,
605 **129**, 2897–2925.

606 Waliser, D. E., 2005: Predictability and Forecasting. *"Intraseasonal Variability of the*
607 *Atmosphere-Ocean Climate System"*, W. K. M. Lau and D. E. Waliser, Eds., Springer,
608 Heidelberg, Germany, 474.

609 Wang, B., and H. L. Rui, 1990: Synoptic climatology of transient tropical intraseasonal
610 convective anomalies: 1975-1985. *Meteor. Atmos. Phys.*, **44**, 43-61.

611 Wang, W., M. Chen, A. Kumar, and Y. Xue, 2011: How important is intraseasonal surface wind
612 variability to real-time ENSO prediction? *Geophys. Res. Lett.*, **38**, L13705,
613 doi:10.1029/2011GL047684.

614 Wang, W., and M. E. Schlesinger, 1999: The dependence on convective parameterization of the
615 tropical oscillation simulated by the UIUC 11-layer atmosphere GCM. *J. Climate*, **12**, 1423–
616 1475.

617 Watanabe, M., and Coauthors, 2010: Improved Climate Simulation by MIROC5: Mean state,
618 variability, and climate sensitivity. *J. Climate*, **23**, 6312–6335.

619 Watanabe, S., and Coauthors, 2011: MIROC-ESM 2010: model description and basic results of
620 CMIP5-20c3m experiments. *Geosci. Model Dev.*, **4**, 845–872. doi:10.5194/gmd-4-845-
621 2011.

622 Weaver, S. J., W. Wang, M. Chen, and A. Kumar, 2011: Representation of MJO variability in
623 the NCEP Climate Forecast System. *J. Climate*, **24**, 4676–4694.

624 Weickmann, K. M., G. R. Lussky, and J. E. Kutzbach, 1985: Intraseasonal (30-60 day)
625 fluctuations of outgoing longwave radiation and 250 mb streamfunction during northern
626 winter. *Mon. Wea. Rev.*, **113**, 941–961.

627 Weickmann, K., G. Kiladis and P. Sardeshmukh, 1997: The dynamics of intraseasonal
628 atmospheric angular momentum oscillations. *J. Atmos. Sci.*, **54**, 1445–1461 .

629 Wheeler, M., and H. H. Hendon, 2004: An all-season real-time multivariate MJO index:
630 Development of an index for monitoring and prediction. *Mon. Wea. Rev.*, **132**, 1917-1932.

631 Wheeler, M. C., and J. L. McBride, 2005: Australian-Indonesian monsoon. *Intraseasonal*
632 *Variability in the Atmosphere-Ocean Climate System*. W.K.M. Lau and D.E. Waliser
633 (Eds.), Praxis Publishing, pp 125-173.

634 Wheeler, M., G. N. Kiladis, 1999: Convectively coupled equatorial waves: Analysis of clouds
635 and temperature in the wavenumber-frequency domain. *J. Atmos. Sci.*, **56**, 374–399.

636 Wheeler, M., and K. M. Weickmann, 2001: Real-time monitoring and prediction of modes of
637 coherent synoptic to intraseasonal tropical variability. *Mon. Wea. Rev.*, **129**, 2677–2694 .

638 Yasunari, T., 1979: Cloudiness fluctuations associated with the northern hemisphere summer
639 monsoon. *J. Meteor. Soc. Japan*, **57**, 227–242.

640 Zhang, C., 2005: Madden-Julian Oscillation, *Rev. Geophys.*, **43**, RG2003,
641 doi:10.1029/2004RG000158.

642 Zhang, C., and M. Dong, 2004: Seasonality in the Madden-Julian Oscillation. *J. Climate*, **17**,
643 3169-3180.

644 Zhang, G. J., and X. Song, 2009: Interaction of deep and shallow convection is key to Madden-
645 Julian Oscillation simulation. *Geophys. Res. Lett.*, **36**, L09708,
646 doi:10.1029/2009GL037340.

647 Zhang, C., M. Dong, S. Gualdi, H. H. Hendon, E. D. Maloney, A. Marshall, K. R. Sperber, and
648 W. Wang, 2006: Simulations of the Madden-Julian oscillation in four pairs of coupled and
649 uncoupled global momdels. *Climate Dyn.*, **27**, 753–592.

650 Zhou, L., R. Neale, M. Jochum, and R. Murtugudde, 2012: Improved Madden–Julian oscillations
651 with improved physics: The impact of modified convection parameterization. *J Climate*,
652 **25**, 1116–1136.

653

654

FIGURE CAPTIONS

Fig. 1 Annual mean precipitation along the equatorial belt averaged between (a) 15°N and 15°S, and (b) 5°N and 5°S for two observational datasets and 20 models. The data are smoothed zonally to retain only wavenumber 0-6. The locations of continents within the equatorial belt are indicated by black bars under the abscissa.

Fig. 2 Variance of the 2-128 day precipitation anomaly along the equator averaged between (a) 15°N-15°S, and (b) 5°N-5°S.

Fig. 3 Space-time spectrum of 15°N-15°S symmetric component of precipitation. Frequency spectral width is 1/128cpd.

Fig. 4 Space-time spectrum of the 15°N-15°S symmetric component of precipitation divided by the background spectrum. Superimposed are the dispersion curves of the odd meridional mode numbered equatorial waves for the five equivalent depths of 8, 12, 25, 50, and 90 m. Frequency spectral width is 1/128 cpd.

Fig. 5 As in Fig. 4 except for the 15°N-15°S antisymmetric component of precipitation.

Fig. 6 Variances of (a) Kelvin, (b) ER, (c) MRG, (d) EIG, and (e) WIG modes along the equator averaged between 15°N and 15°S.

Fig. 7 Variance of the MJO mode along the equator averaged between (a) 15°N and 15°S, and (b) 5°N and 5°S.

Fig. 8 Ratio between the MJO variance and the variance of its westward counterpart (westward wavenumber 1-6, 30-70 day mode). The variances are averaged over (a) an Indian Ocean box between 5°N-5°S and 70°E-10°E, and (b) a western Pacific box between 5°N-5°S and 140°E-170°E.

Fig. 9 Lag correlation of the 30-70-day precipitation anomaly averaged along the equator between 5°N and 5°S with respect to itself at 0°, 85°E. The three lines correspond to phase speed of 3, 7, and 15 m s⁻¹, respectively.

Fig. 10 Normalized spectrum of the eastward wavenumber 1-6 component of equatorial precipitation (5°N-5°S) at 0°, 85°E for two observational datasets and 14 models. Frequency spectral width is 1/100 cpd.

Fig. 11 Auto-correlation of precipitation at 0°, 85°E.

685

686

687 **Table 1 List of models that participate in this study**

Institute	IPCC ID	Label in figures	Gridpoint/ resolution/ model top	Deep convection scheme / Modification	Closure/ Trigger
Canadian Centre for Climate Modelling and Analysis (CCCma)	CanCM4	CanCM4	Spectral/T63 × L35/1 hPa	Zhang & McFarlane (1995)	CAPE
Canadian Centre for Climate Modelling and Analysis (CCCma)	CanESM2	CanESM2	Spectral/T63 × L35/1 hPa	Zhang & McFarlane (1995)	CAPE
National Center for Atmospheric Research (NCAR)	CCSM4	CCSM4	Grid point/288 × 200 × L26	Zhang & McFarlane (1995)/ Neale et al. (2008)	Diluted CAPE
Centre National de Recherches Meteorologiques/Centre Europeen de Recherche et Formation Avanceess en Calcul Scientifique (CNRM/CERFACS)	CNRM-CM5	CNRM-CM5	Spectral/T127(1.4°) × L91/10 hPa	Bougeault (1985)	Moisture convergence
Commonwealth Scientific and Industrial Research Organisation in collaboration with the Queensland Climate Change Centre of Excellence	CSIRO-Mk3.6.0	CSIRO	Spectral/T63 (1.875°) × L18/	Gregory and Rowntree (1990)/Gregory (1995)	Cloud base buoyancy
Institute for Numerical Mathematics (INM)	INM-CM4	INMCM4	Grid point/180 × 120 × L21/	Betts (1986)	CAPE
Institut Pierre-Simon Laplace (IPSL)	IPSL-CM5A-LR	IPSL-5AL	Grid point/143 × 144 × L39/	Emanuel (1991)	CAPE
Institut Pierre-Simon Laplace (IPSL)	IPSL-CM5A-MR	IPSL-5AM	Grid point/143 × 144 × L39/	Emanuel (1991)	CAPE
Institut Pierre-Simon Laplace (IPSL)	IPSL-CM5B-LR	IPSL-5BL	Grid point/96 × 96 × L39/	Grandpeix and Lafore (2010)	
LASG, Institute of Atmospheric Physics, Chinese Academy of Sciences (LASG-IAP)	FGOALS-s2	FGOALS	Specral/R42 × L26/2.19 hPa	Tiedtke (1989) / Nordeng (1994)	CAPE/ Moisture convergence
Atmosphere and Ocean Research Institute (The University of	MIROC4h	MIROC4h	Specral/T213	Pan and Randall (1998)	CAPE/ Relative

Tokyo), National Institute for Environmental Studies, and Japan Agency for Marine-Earth Science and Technology (MIROC)			$(0.6^\circ) \times L56/$	/ Emori et al. (2001)	humidity
Atmosphere and Ocean Research Institute (The University of Tokyo), National Institute for Environmental Studies, and Japan Agency for Marine-Earth Science and Technology (MIROC)	MIROC5	MIROC5	Spectral/T85 $(1.4^\circ) \times L40/0.003 \text{ hPa}$	Chikira and Sugiyama (2010)/ Pan and Randall (1998)	CAPE
Japan Agency for Marine-Earth Science and Technology, Atmosphere and Ocean Research Institute (The University of Tokyo), and National Institute for Environmental Studies	MIROC-ESM	MIROC-E	Spectral/T42 $(2.8^\circ) \times L80/0.003 \text{ hPa}$	Pan and Randall (1998) / Emori et al. (2001)	CAPE/ Relative humidity
Japan Agency for Marine-Earth Science and Technology, Atmosphere and Ocean Research Institute (The University of Tokyo), and National Institute for Environmental Studies	MIROC-ESM-CHEM	MIROC-EC	Spectral/T42 $(2.8^\circ) \times L80/0.003 \text{ hPa}$	Pan and Randall (1998) / Emori et al. (2001)	CAPE/ Relative humidity
Met Office Hadley Centre (MOHC)	HadCM3	HadCM3	Spectral /T42 $\times L19/$	Gregory and Rowntree (1990)	Cloud base buoyancy
Met Office Hadley Centre (MOHC)	HadGEM2-CC	HadG2-CC	Grid point/192 $\times 145 \times L38$	Gregory and Rowntree (1990)	Cloud base buoyancy
Met Office Hadley Centre (MOHC)	HadGEM2-ES	HadG2-ES	Grid point/192 $\times 145 \times L38$	Gregory and Rowntree (1990)	Cloud base buoyancy
Max Planck Institute for Meteorology (MPI-M)	MPI-ESM-LR	MPI-E-L	Spectral/T63 $\times L47/0.01 \text{ hPa}$	Tiedtke (1989) / Nordeng (1994)	CAPE/ Moisture convergence
Meteorological Research Institute	MRI-CGCM3	MRI3	Spectral/T42 $\times L46/0.01 \text{ hPa}$	Pan and Randall (1998)	CAPE
Norwegian Climate Centre (NCC)	NorESM1-M	NroE1-M	Grid point/ $1.9^\circ \times 2.5^\circ \times L26$	Zhang & McFarlane (1995)/ Neale et al. (2008)	Diluted CAPE

688

689

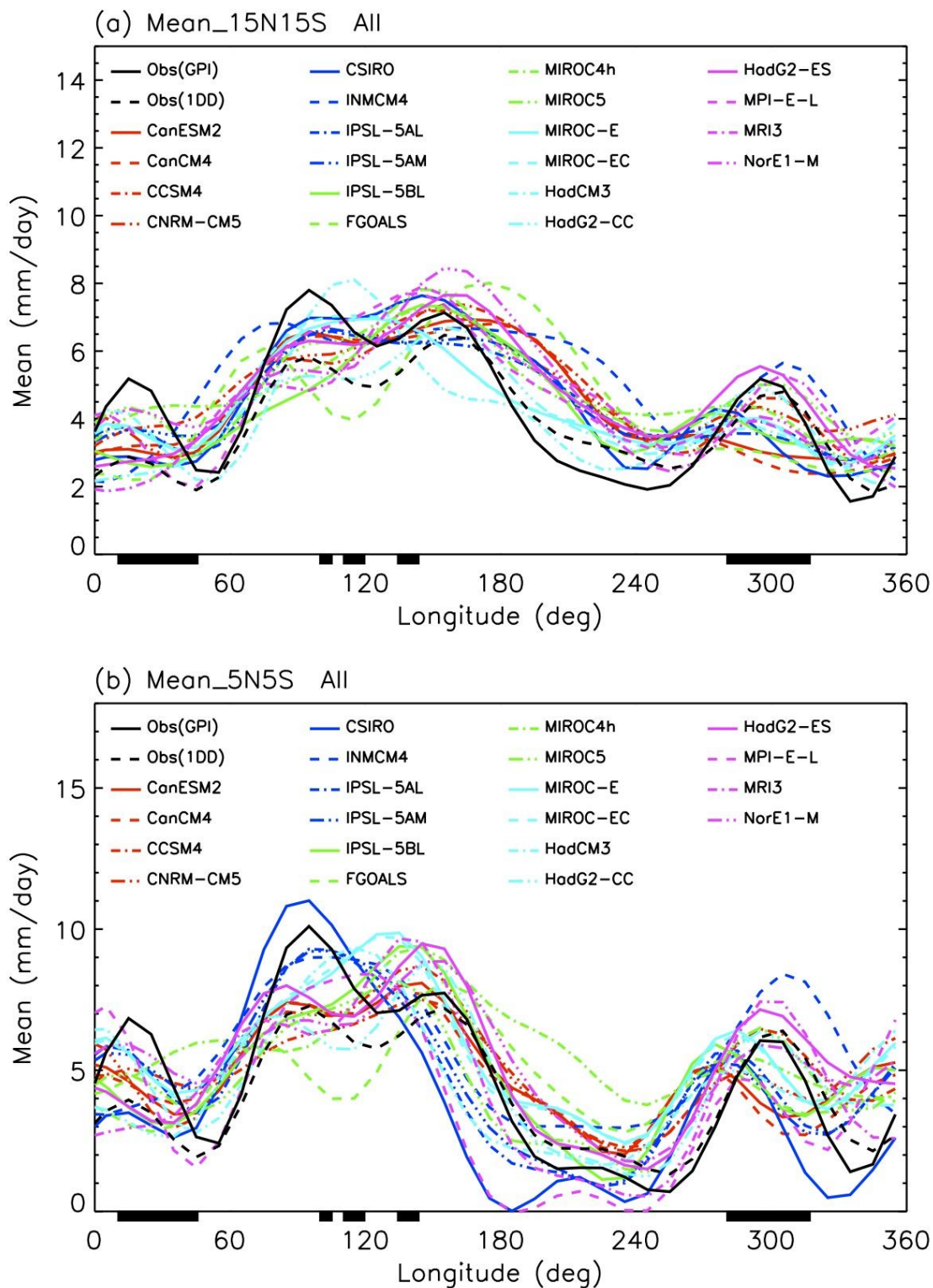


Fig. 1 Annual mean precipitation along the equatorial belt averaged between (a) 15°N and 15°S, and (b) 5°N and 5°S for two observational datasets and 20 models. The data are smoothed zonally to retain only wavenumber 0-6. The locations of continents within the equatorial belt are indicated by black bars under the abscissa.

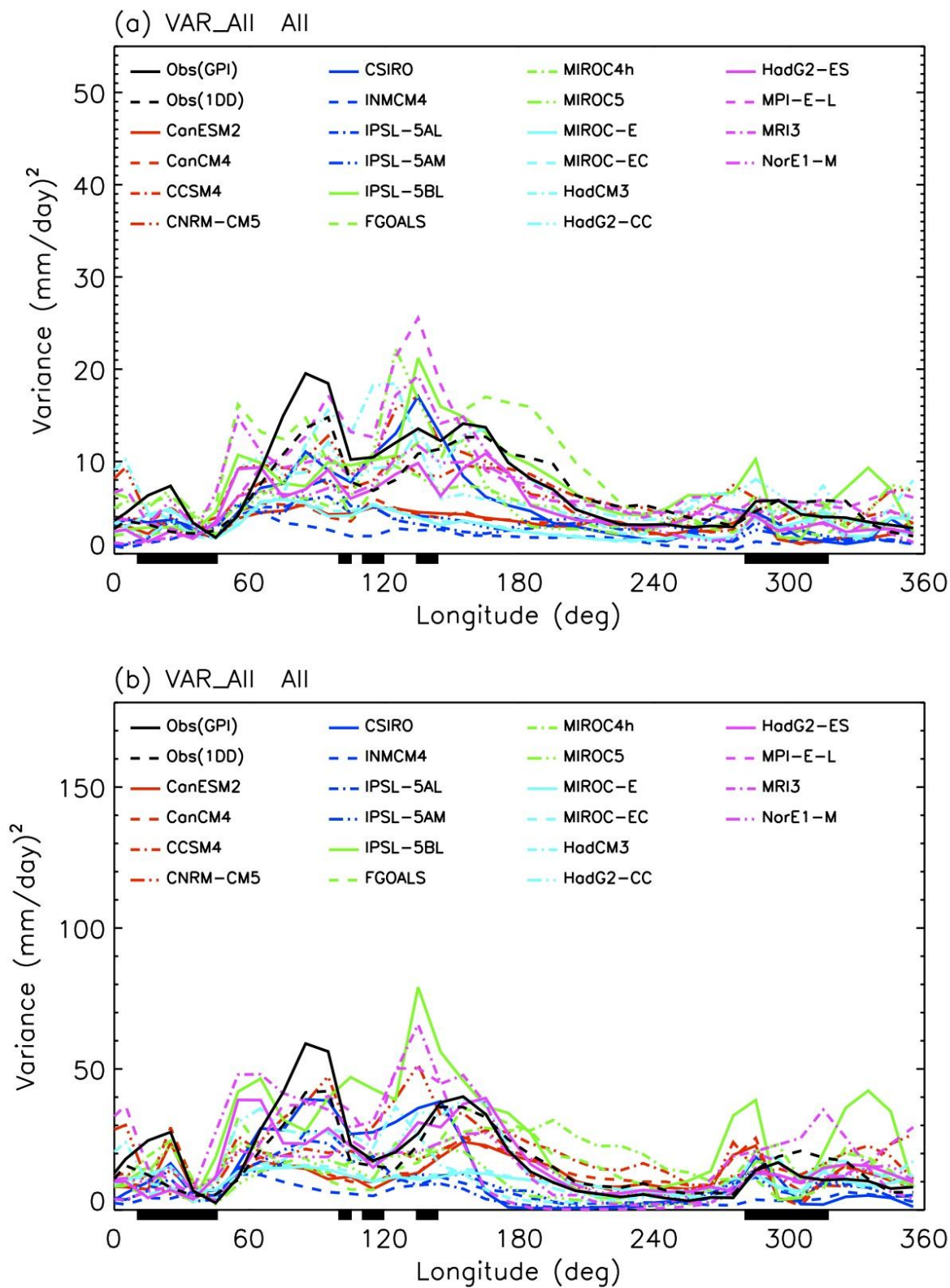


Fig. 2 Variance of the 2-128 day precipitation anomaly along the equator averaged between (a) 15°N-15°S, and (b) 5°N-5°S.

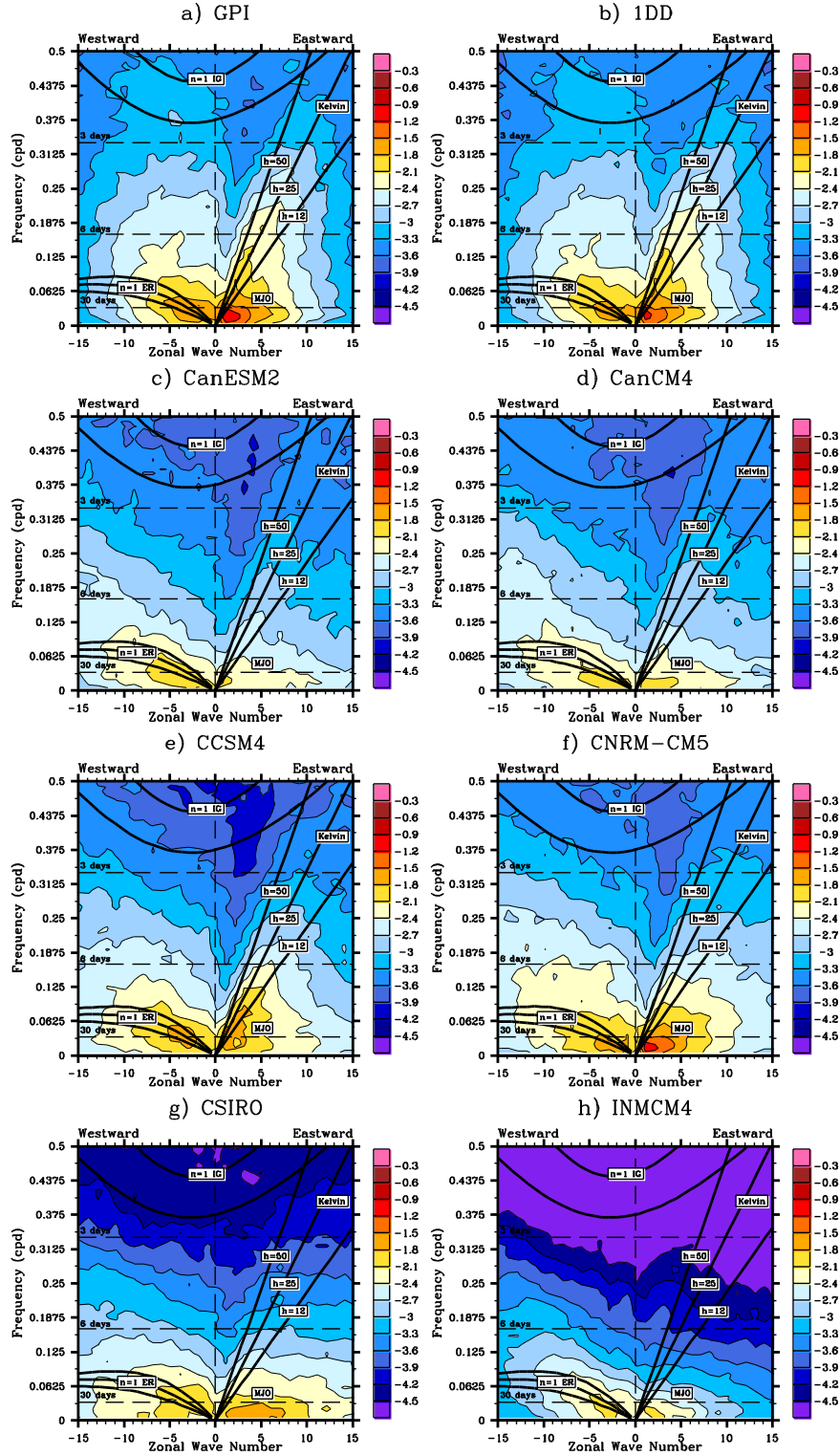


Fig. 3 Space-time spectrum of 15°N-15°S symmetric component of precipitation. Frequency spectral width is 1/128cpd.

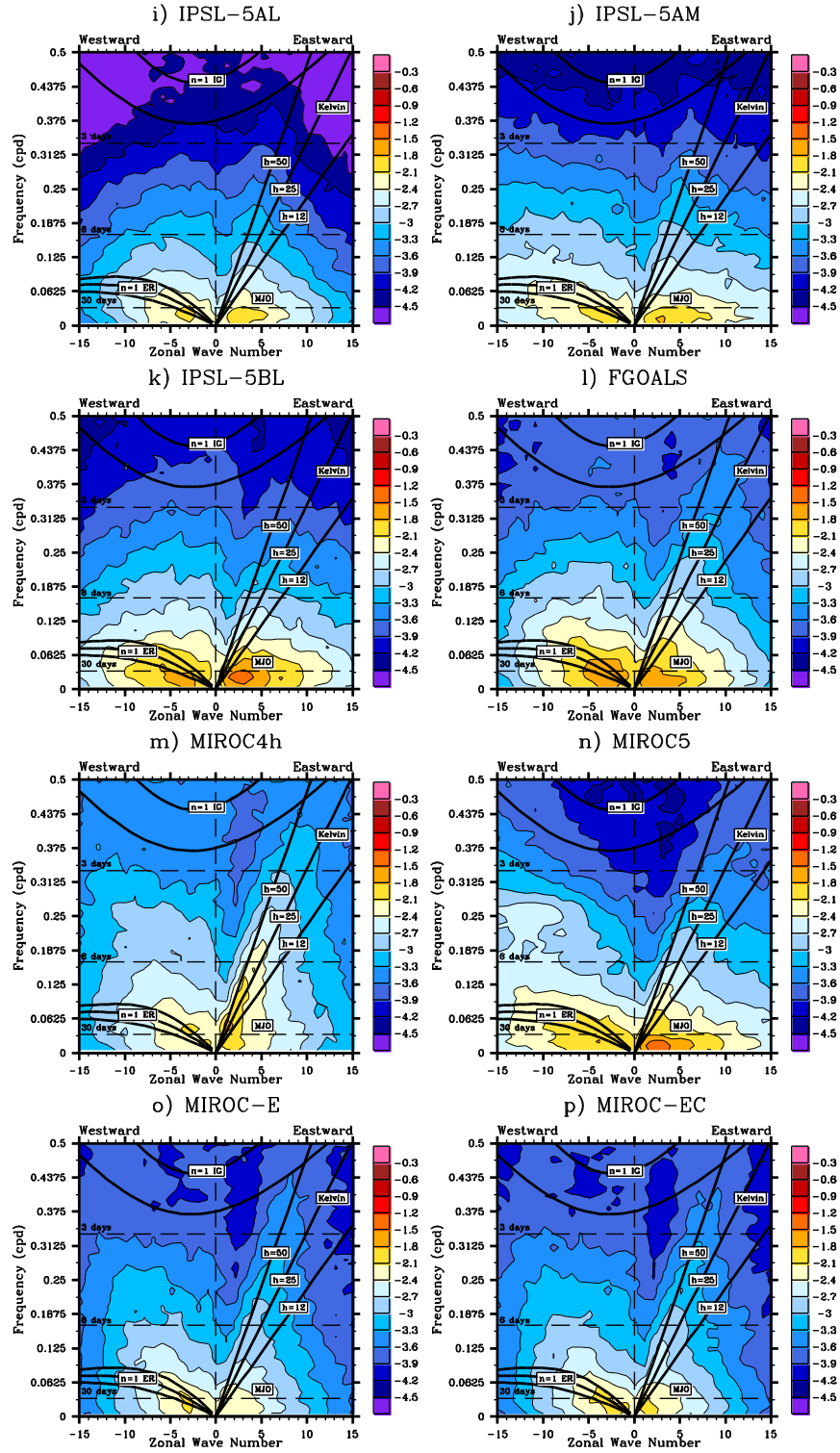


Fig. 3 (Continued)

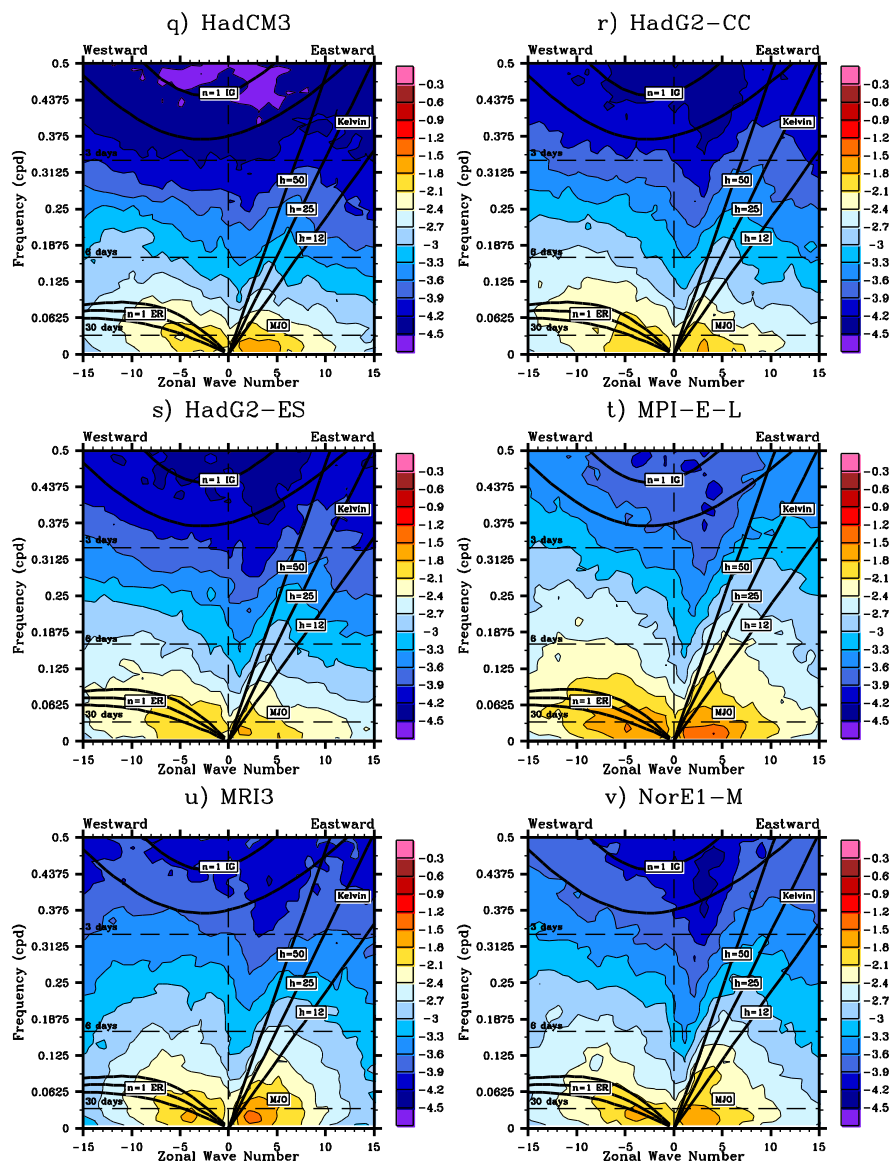


Fig. 3 (Continued)

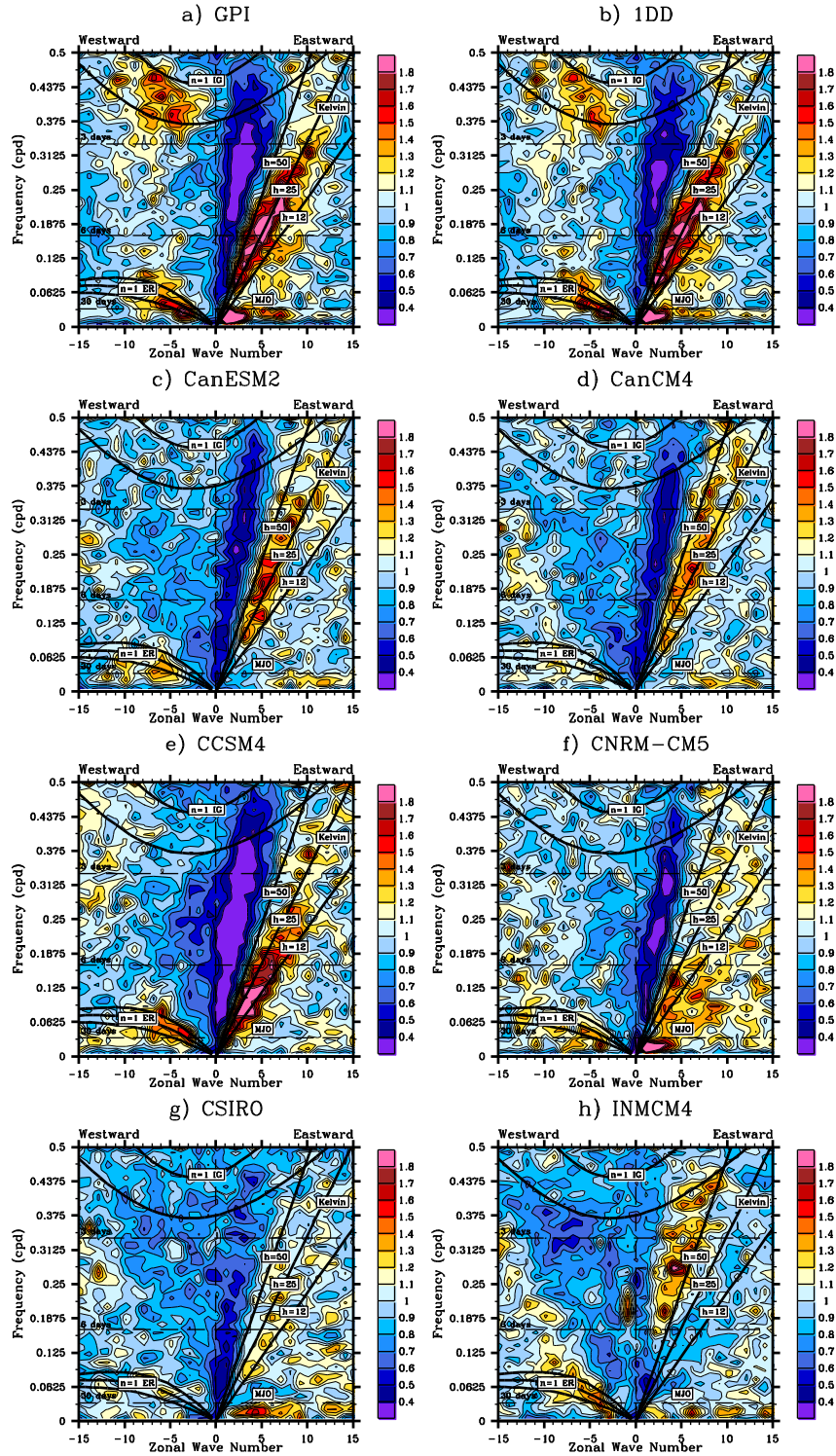


Fig. 4 Space –time spectrum of the 15°N-15°S symmetric component of precipitation divided by the background spectrum. Superimposed are the dispersion curves of the odd meridional mode numbered equatorial waves for the five equivalent depths of 8, 12, 25, 50, and 90 m. Frequency spectral width is 1/128 cpd.

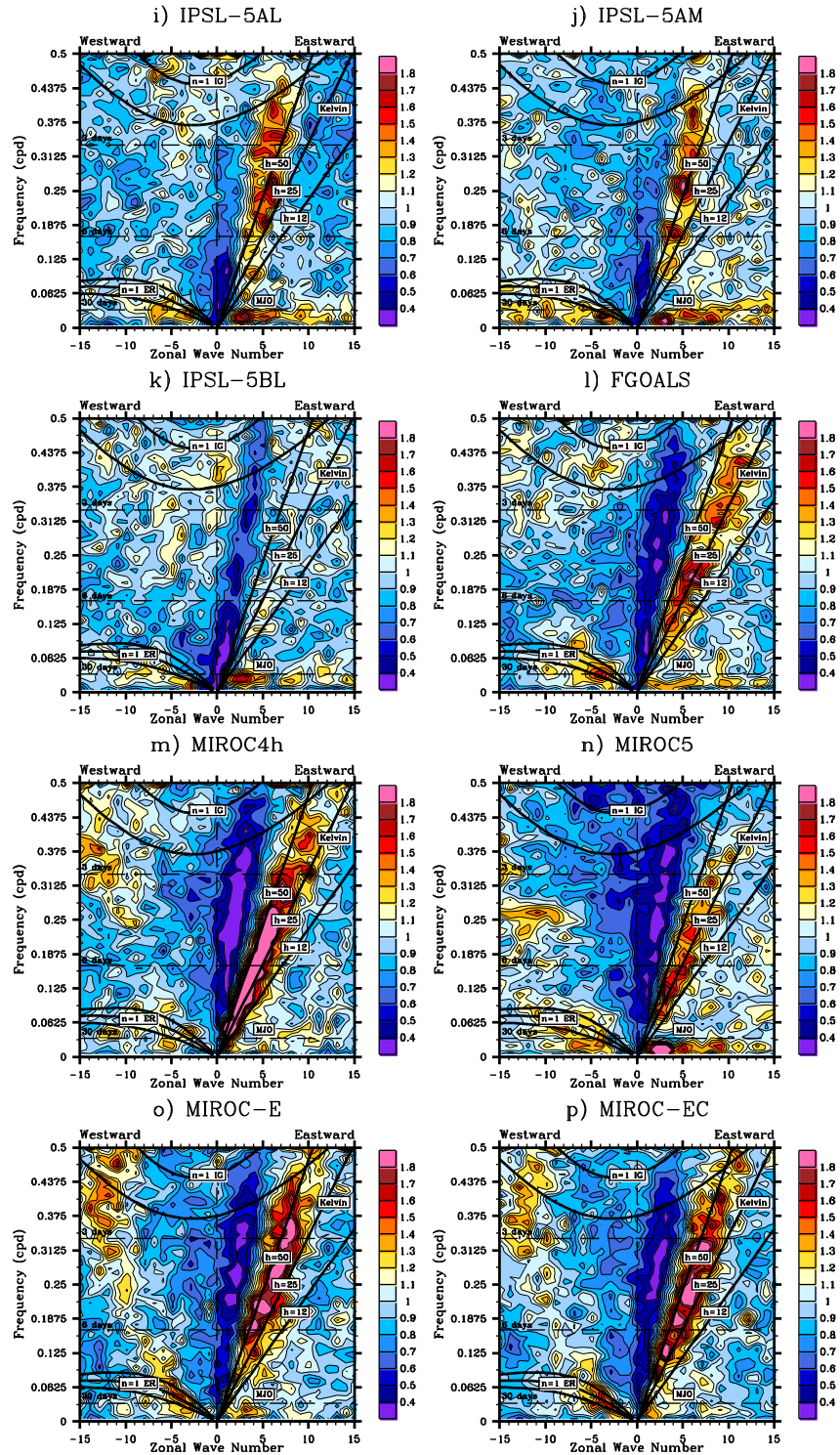


Fig. 4 (Continued)

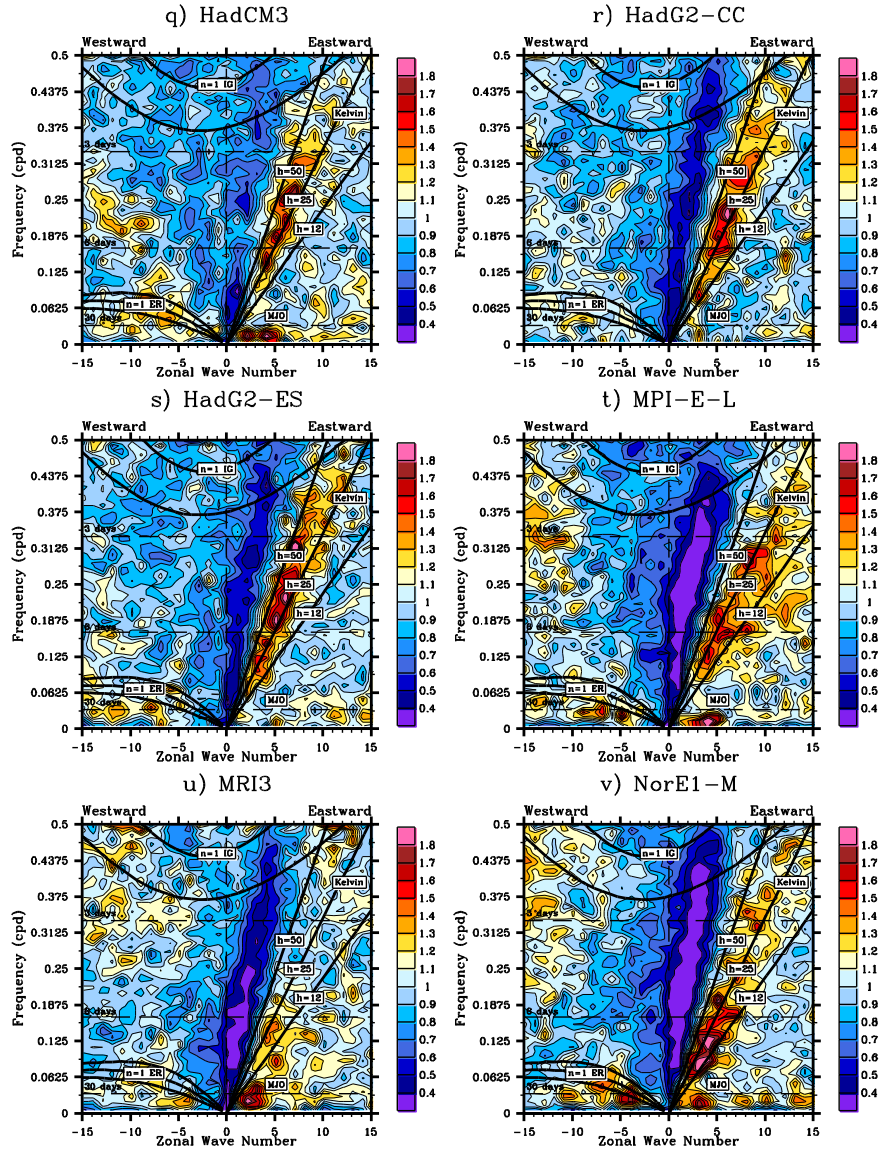


Fig. 4 (Continued)

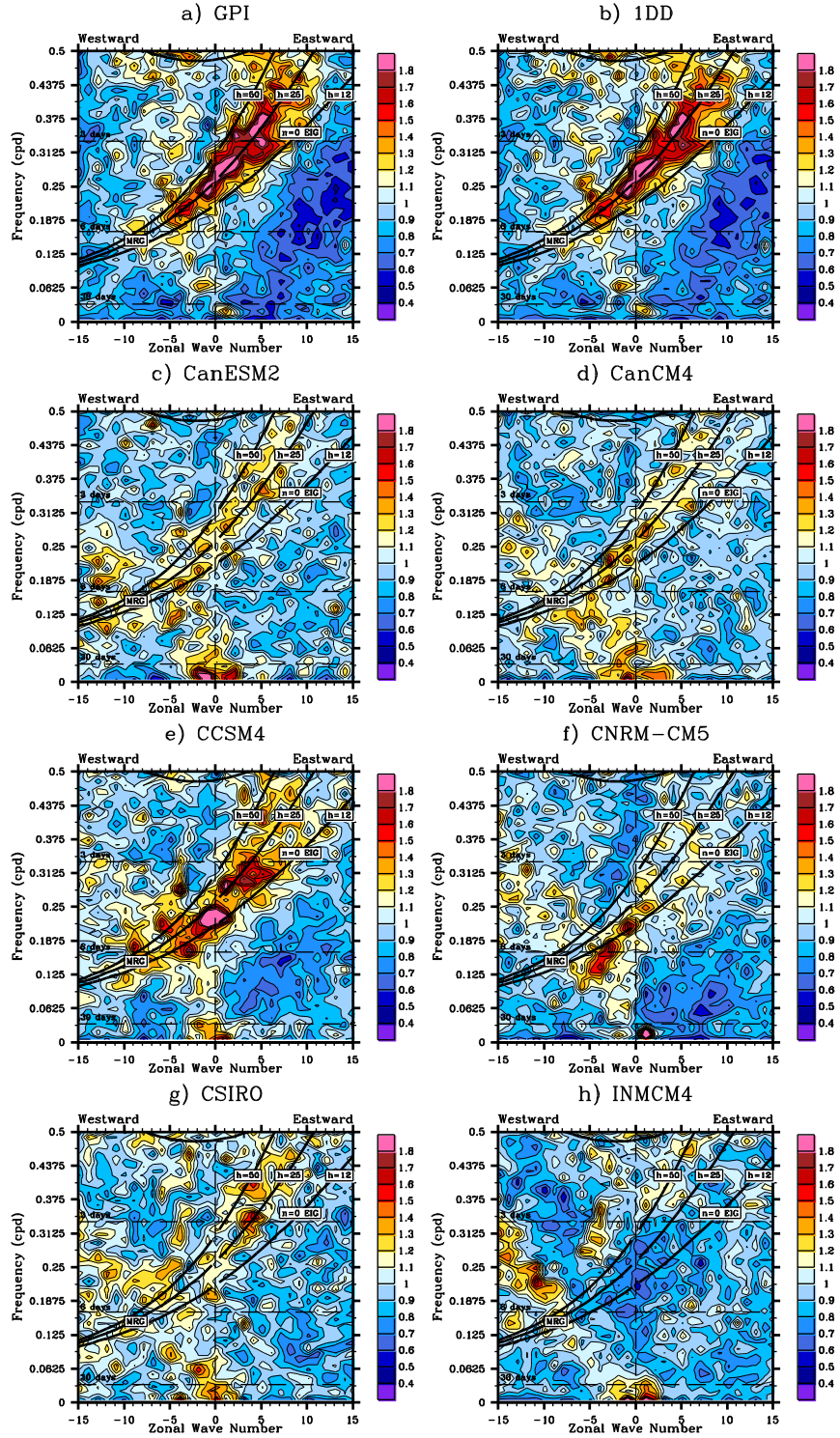


Fig. 5 As in Fig. 4 except for the 15°N-15°S antisymmetric component of precipitation.

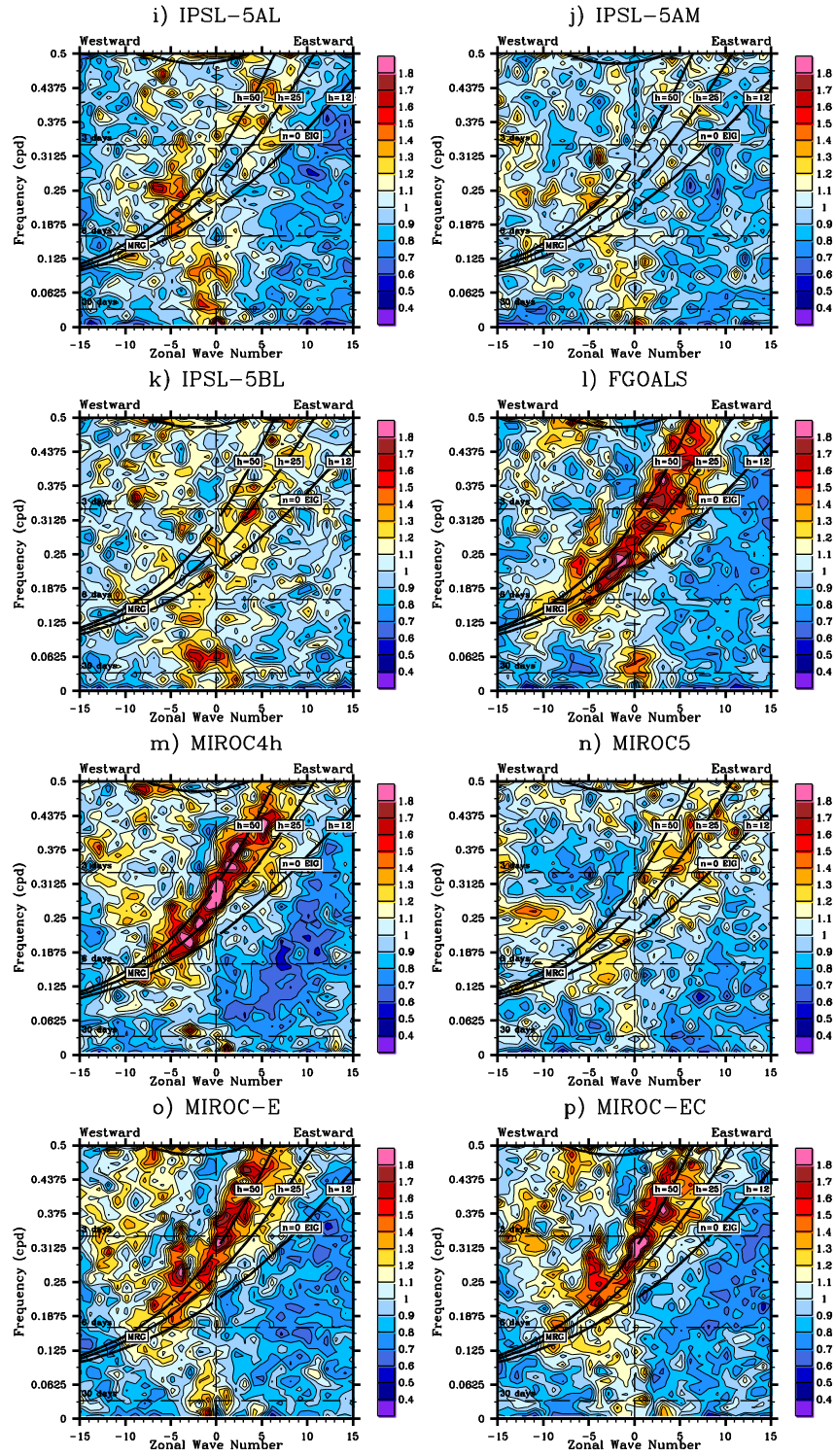


Fig. 5 (Continued)

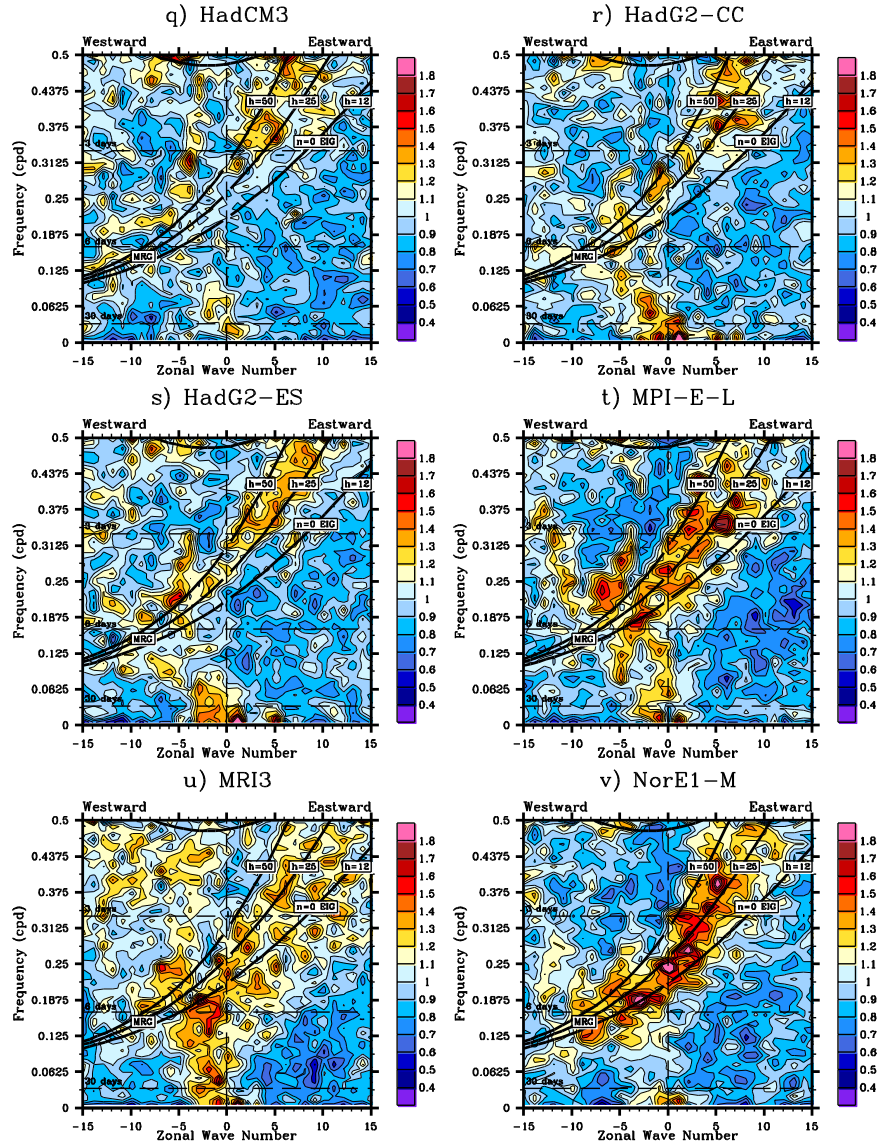


Fig. 5 (Continued)

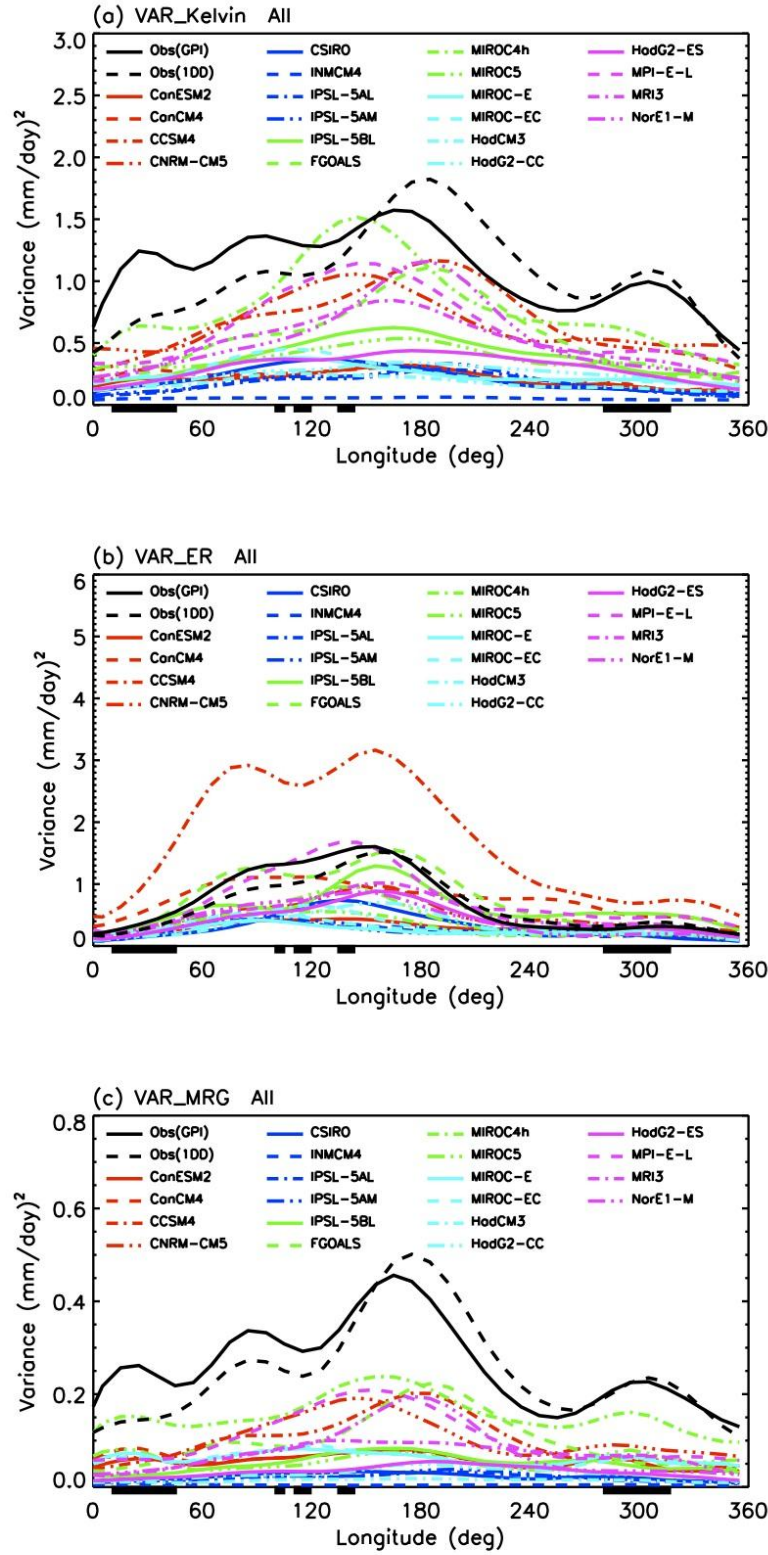


Fig. 6 Variances of (a) Kelvin, (b) ER, (c) MRG, (d) EIG, and (e) WIG modes along the equator averaged between 15°N and 15°S.

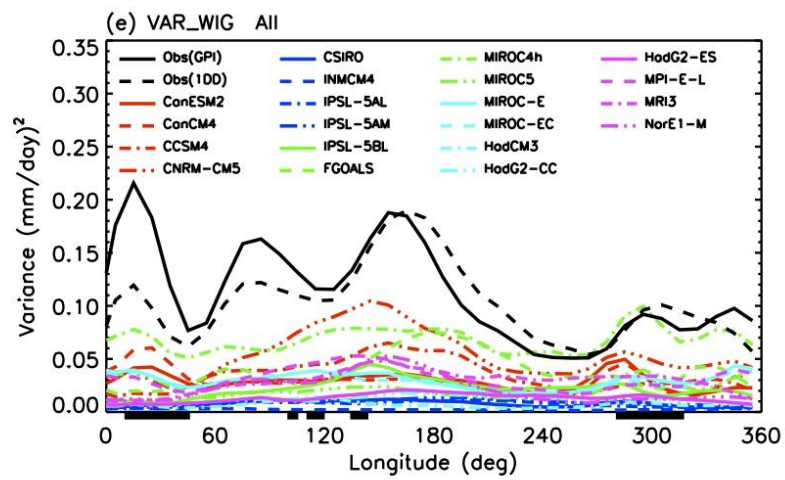
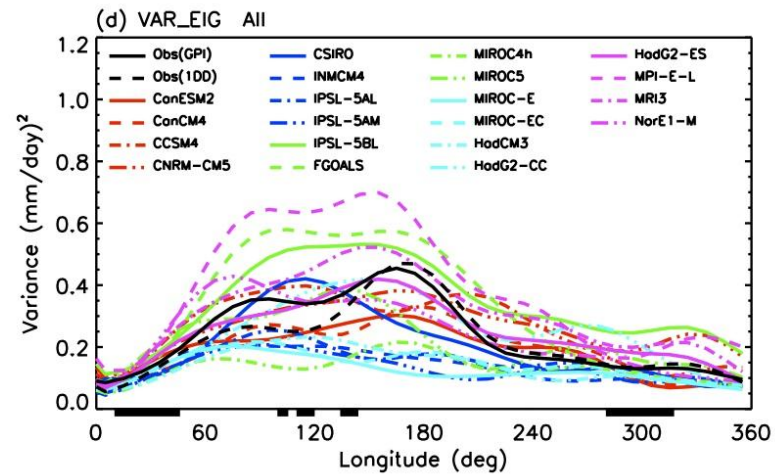


Fig. 6 (Continued)

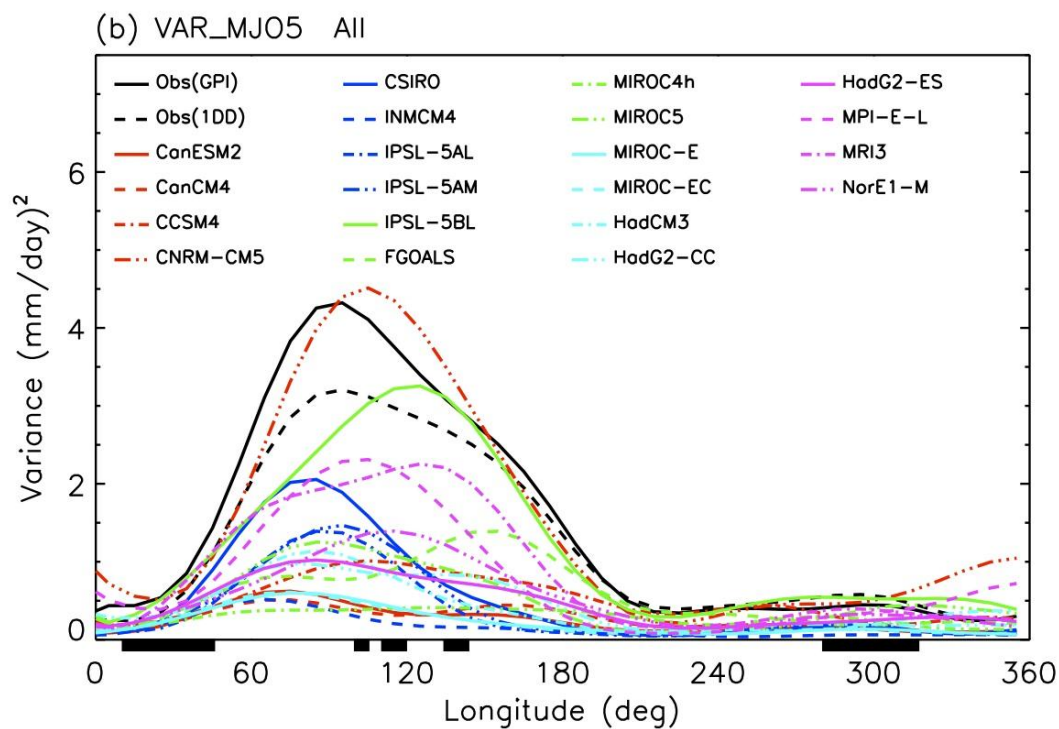
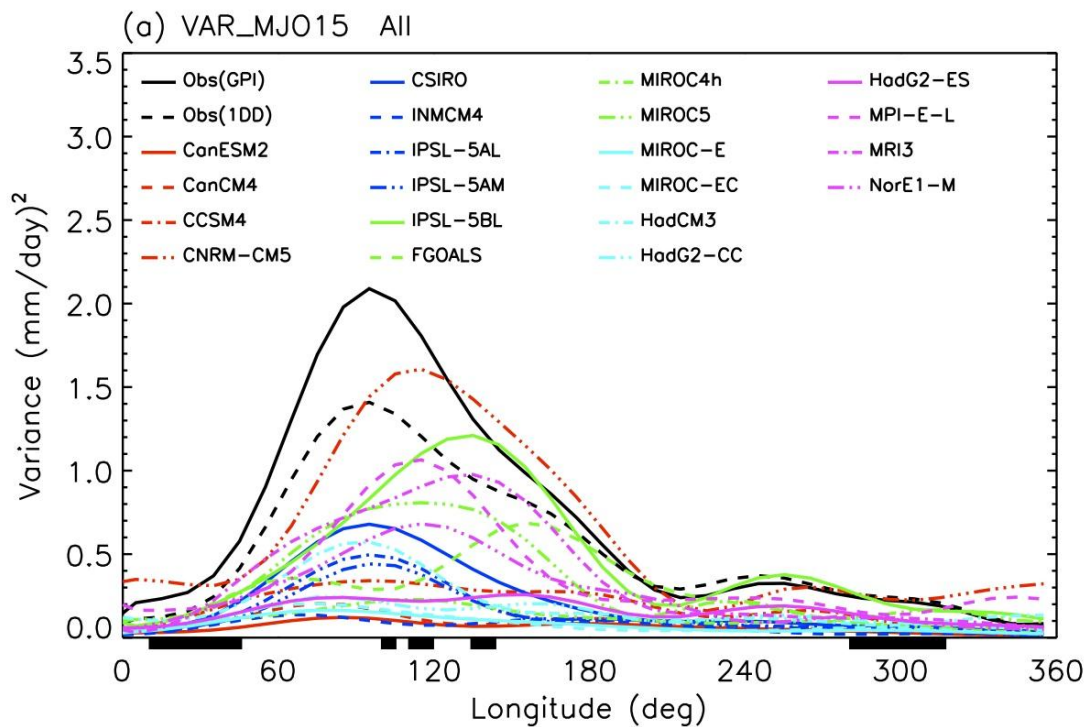


Fig. 7 Variance of the MJO mode along the equator averaged between (a) 15°N and 15°S, and (b) 5°N and 5°S.

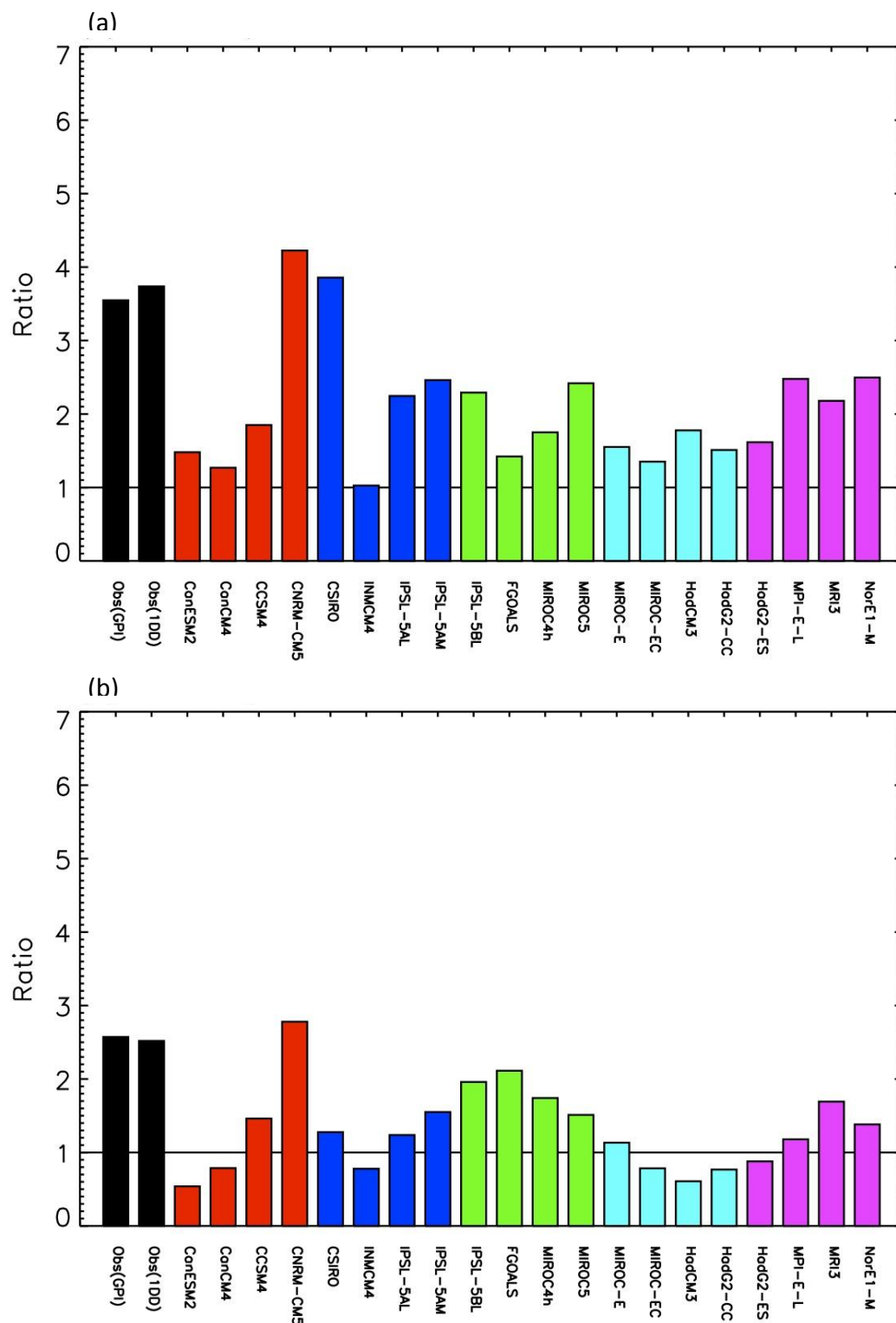


Fig. 8 Ratio between the MJO variance and the variance of its westward counterpart (westward wavenumber 1-6, 30-70 day mode). The variances are averaged over (a) an Indian Ocean box between 5°N-5°S and 70°E-10°E, and (b) a western Pacific box between 5°N-5°S and 140°E-170°E.

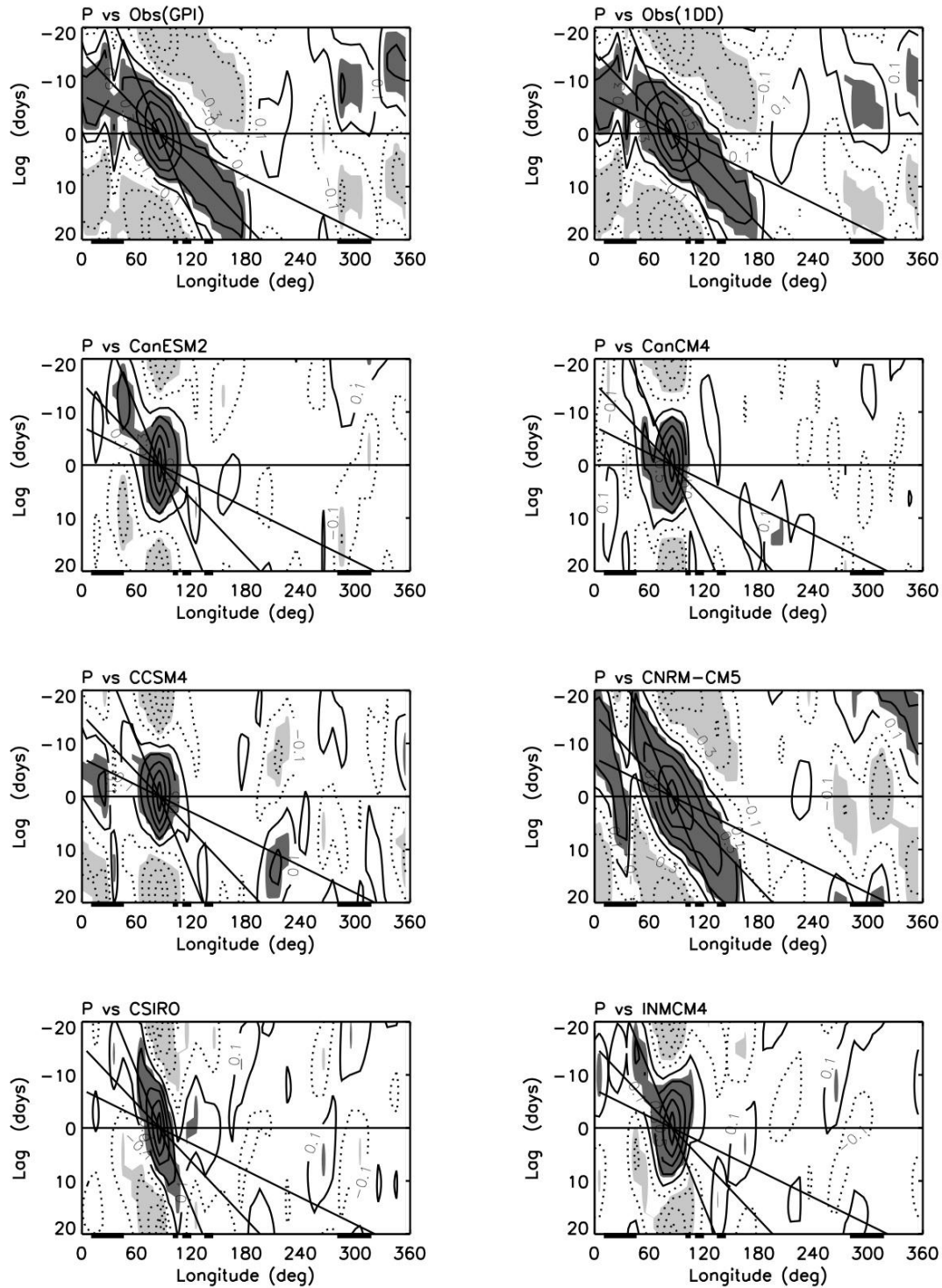


Fig. 9 Lag correlation of the 30-70-day precipitation anomaly averaged along the equator between 5°N and 5°S with respect to itself at 0°, 85°E. The three lines correspond to phase speed of 3, 7, and 15 m s⁻¹, respectively.

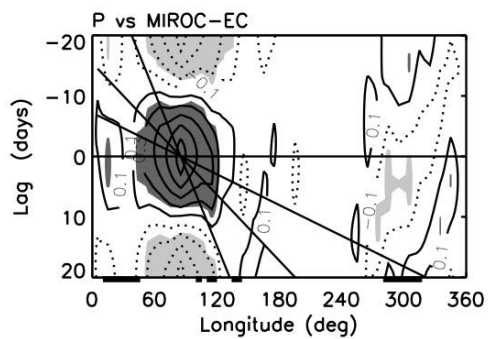
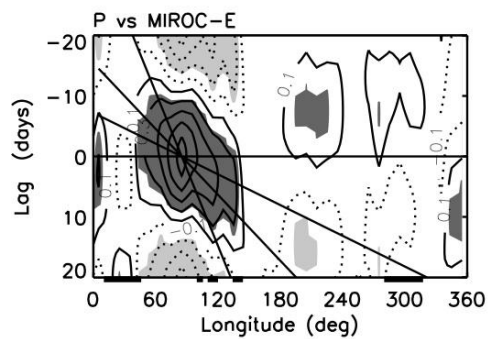
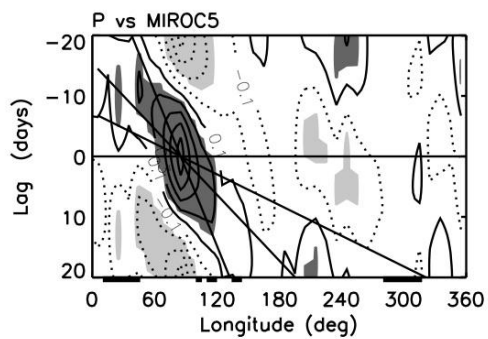
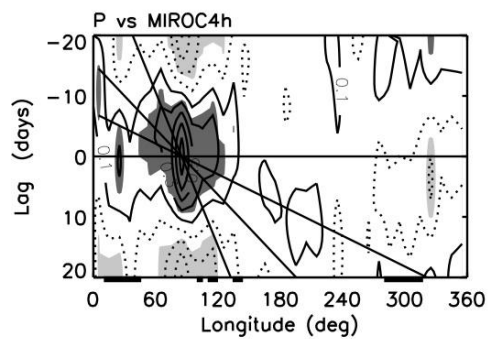
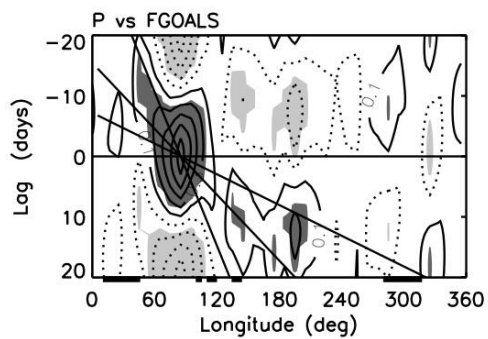
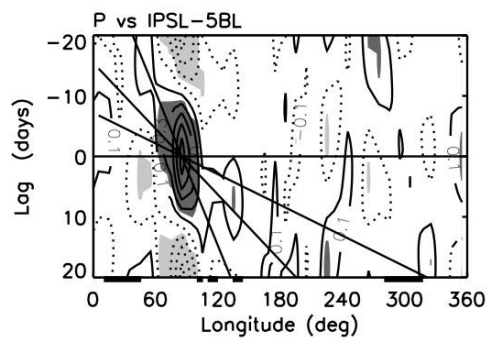
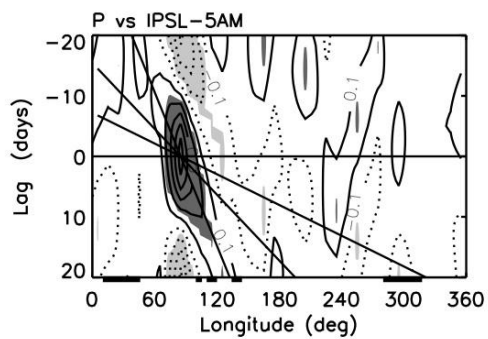
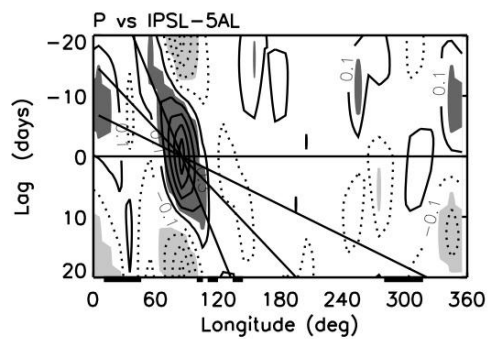


Fig. 9 (Continued)

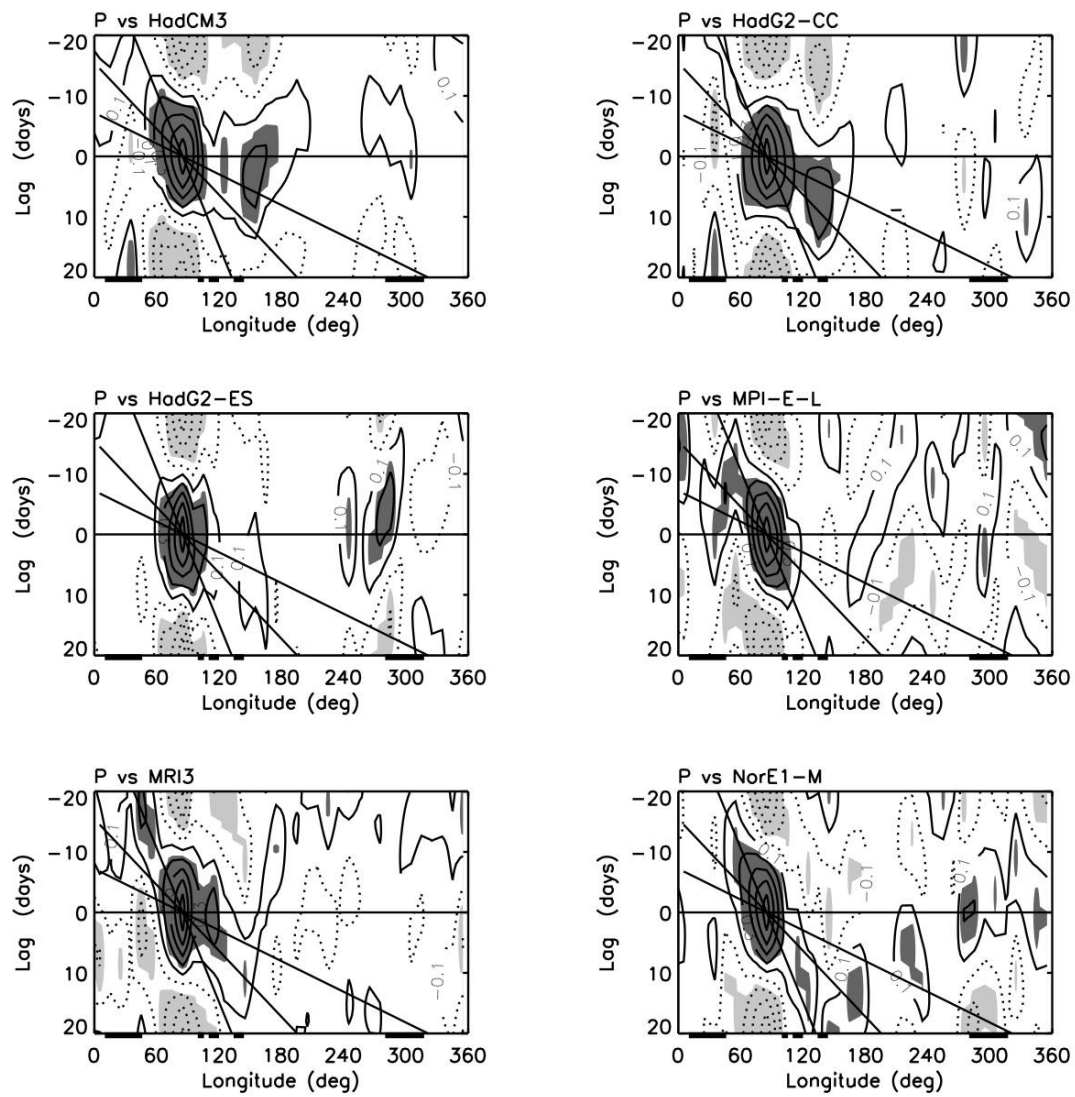


Fig. 9 (Continued)

735

736

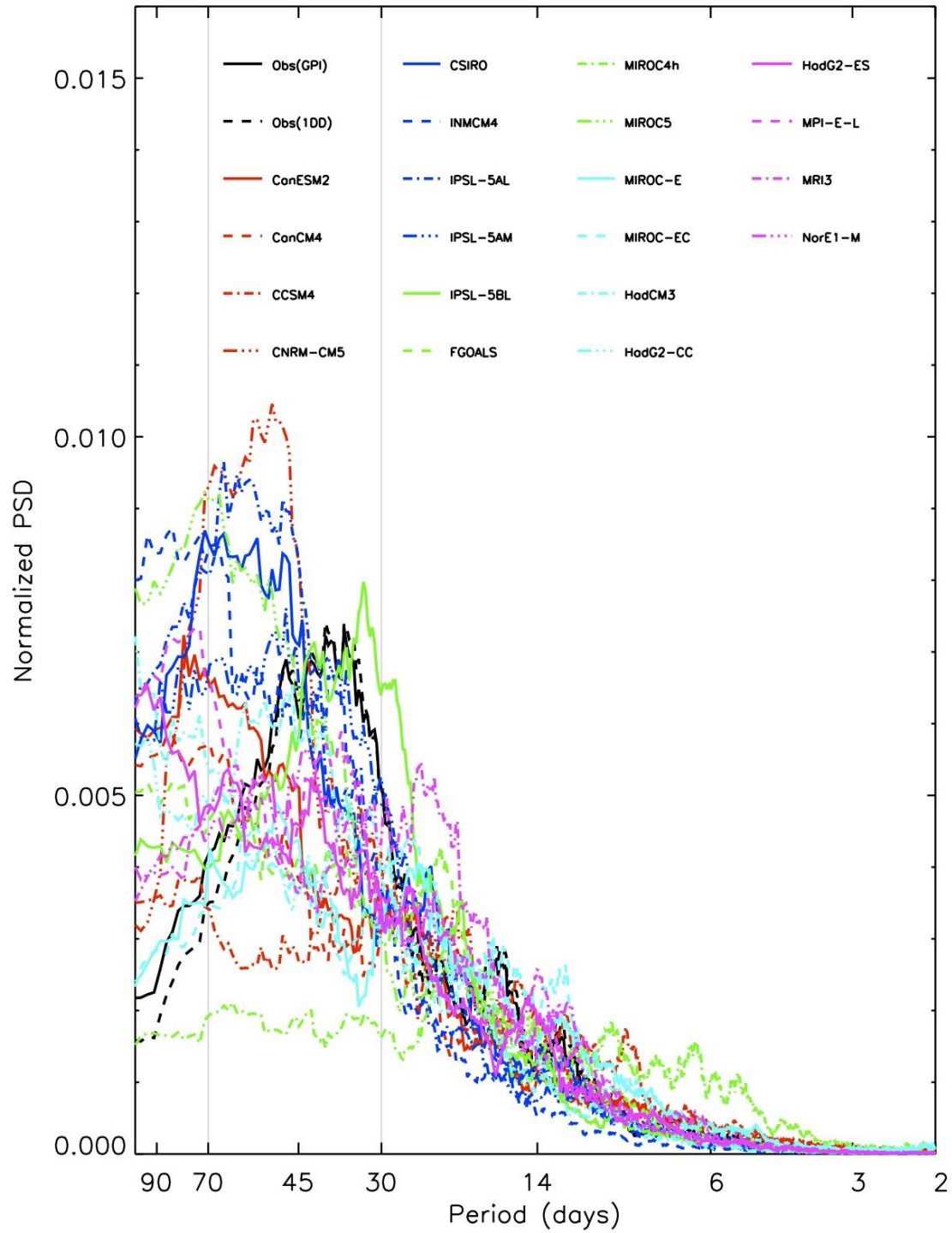


Fig. 10 Normalized spectrum of the eastward wavenumber 1-6 component of equatorial precipitation (5°N - 5°S) at 0° , 85°E for two observational datasets and 14 models. Frequency spectral width is $1/100$ cpd.

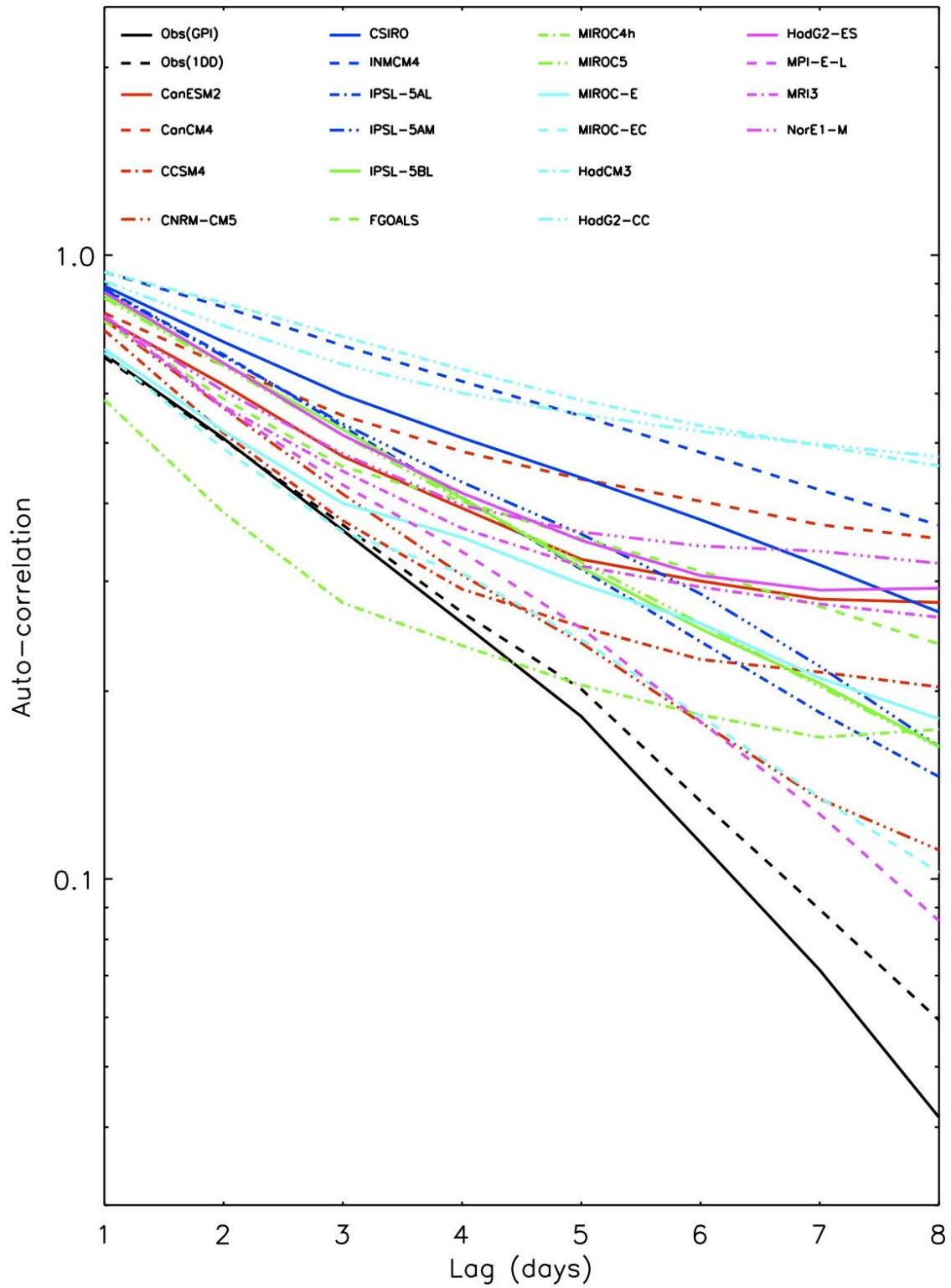


Fig. 11 Auto-correlation of precipitation at 0°, 85°E.